

Electronic Supplementary Information

The Impact of Second Coordination Sphere Functional Group Extension on Product Selectivity for Manganese Bipyridyl CO₂ Reduction Electrocatalysts

Lisa Suntrup^a, Vanna Blaszczak^a, Roonak Saeedi^a, Mehmed Z. Ertem^b, Jonathan Rochford^{a*}

^aDept. of Chemistry, University of Massachusetts Boston, 100 Morrissey Boulevard, Boston, MA 02125, USA.

^bChemistry Division, Brookhaven National Laboratory, Upton, New York 11973-5000, USA.

Email: jonathan.rochford@umb.edu

Table of Contents

1.	<u>Experimental</u>	2
	<i>i.</i> <u>Materials and methods</u>	2
	<i>ii.</i> <u>Synthesis</u>	5
2.	<u>Computational methods</u>	10
3.	<u>High-resolution mass spectrometry data</u>	11
4.	<u>NMR spectrometry data</u>	13
5.	<u>Cyclic voltammetry under 1 atm argon</u>	19
6.	<u>Infrared spectroelectrochemistry</u>	23
7.	<u>Voltammetry under 1 atm CO₂</u>	25
8.	<u>Computational data and transition state structures</u>	39
9.	<u>References</u>	42

1. Experimental

i. Materials and Methods

The following chemicals were purchased from Sigma Aldrich; bromopentacarbonylmanganese(I) (98%), silver trifluoromethanesulfonate (>99%), dicyclohexylcarbodiimide (99%), *N,N'*-dimethyl-4-aminopyridine (99%), tetrabutylammonium hexafluorophosphate (>99%), sodium carbonate (>99%), phenol (>99.9%), tetrahydrofuran (reagent grade, 99%), acetonitrile (electronic grade, 99.999%), acetic acid (99%), Boc-L-alanine (99%), 2-methoxybenzoic acid (99%), 2,6-dimethylbenzoic acid (97%). 6,6'-dibromo-2,2'-bipyridine (>95%) was purchased from TCI America. ACS reagent grade dichloromethane, diethyl ether, acetone and diethyl ether were purchased from Pharmco. Tetrabutylammonium hexafluorophosphate was recrystallized thrice from ethanol and dried under vacuum prior to electrolyte preparation in electronic grade acetonitrile.

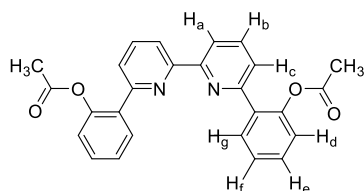
All Mn complexes were prepared in a CEM Discover SP microwave reactor at 80 °C for a 15 min duration in THF solution. It should be highlighted that the microwave reaction tube is sealed airtight in a dark reaction chamber during operation yielding elevated pressure (<6 bar) and dark reaction conditions. Mn polypyridyl complexes are readily accessible by traditional reflux methods in diethyl ether or THF solvent (depending upon ligand solubility),¹ however, due to the light and air sensitivity of Mn polypyridyl complexes inert gas and dark conditions are recommended for an optimal reaction yield. FTIR spectra were recorded on a Thermo Nicolet 670 FTIR spectrophotometer. NMR spectra were recorded on an Agilent spectrometer operated at 399.80 MHz for ¹H nuclei, and 100.54 MHz for ¹³C nuclei. Deuterated solvents CDCl₃ and CD₃CN were used as received from Sigma Aldrich and their residual ¹H and ¹³C solvent signals used as internal references for reporting the ¹H and ¹³C chemical shift (δ) in ppm.² All NMR spectra were recorded

at 20 °C. Liquid chromatography coupled to low resolution mass spectrometry (LC-MS) was performed on an Agilent 2100 system using atmospheric pressure chemical ionization (APCI) mode. High resolution mass spectrometry (HR-MS) was performed on a Thermo Scientific Orbitrap Fusion Lumos using direct injection electrospray ionization. Voltammetry and controlled potential electrolysis were carried out on a CH Instruments 620E potentiostat. A custom three electrode cell was used for both voltammetry and bulk electrolysis experiments allowing airtight introduction of working, counter and reference electrodes as well as needles for gas purging/exhaust. For linear and cyclic voltammetry, a glassy carbon disc (3 mm diameter) and Pt wire were used as working and counter electrodes, respectively, with 0.1 M [Bu₄N][PF₆] in acetonitrile as the supporting electrolyte. A non-aqueous reference electrode was used to minimize ohmic potential drop at the solvent interface. This consisted of a Ag wire in 0.1 M [Bu₄N][PF₆] acetonitrile supporting electrolyte isolated by a Vycor frit, which was calibrated in-situ using the ferrocenium/ferrocene redox couple as a pseudo reference. As redox potentials are often irreversible for the complexes studied, anodic (E_{pa}) and cathodic (E_{pc}) peak potentials are reported accordingly. For electrocatalytic linear sweep voltammetry studies, all observed currents were corrected for a dilution factor of the manganese complex analyte upon addition of various volumes of each Brønsted acid. For controlled potential electrolysis experiments a glassy carbon plate working electrode ($A \sim 1 \text{ cm}^2$) was used. A Pt gauze counter electrode was used, isolated from the main compartment by a fine porosity Vycor[®] frit. Each CPE experiment was conducted for a minimum of three hours. Gas chromatography data was recorded on a custom Shimadzu GC-2014 instrument where a raney-Ni methanizer catalyst was used to convert CO to CH₄ prior to quantification of CH₄ by the flame ionization detector (FID) for improved sensitivity. H₂ was simultaneously monitored during the same injection by a thermal conductivity detector (TCD).

The GC was calibrated for CO and H₂ quantification by mimicking bulk electrolysis conditions (i.e., 5 mL supporting electrolyte in the same cell, with electrodes, under 1 atm CO₂). Standard curves for H₂ and CO were generated using this cell where known volumes of the analyte gases (H₂ and CO) were injected and the solution was stirred for 30 min to allow equilibration of the analyte between the electrolyte and headspace prior to GC injection. Formate quantification was performed by a single injection, after electrolysis was complete, using a Metrohm Enviro Trace ion chromatograph system with a 3.2 mM NaHCO₃/1.0 mM Na₂CO₃ eluent. A 500 mM H₂SO₄ solution was used with the Dosino system for automatic regeneration of the Metrohm Suppressor Module (MSM). Infrared spectroelectrochemical (IRSEC) measurements were carried out in argon saturated 0.1 M [Bu₄N][PF₆] acetonitrile supporting electrolyte with 5 mM analyte using a LabOmak UF-SEC cell with Pt mesh working and counter electrodes, and a Ag wire reference electrode. IRSEC spectra acquisition was conducted after recording a blank which included both electrolyte and the resting oxidation state of the analyte. This method generates a difference spectrum (Δ absorbance) where negative peaks correspond to a reduced concentration of the starting material and positive peaks correspond to the a growth in concentration of the reduction products. In the case where peaks of the reduction products were not fully visible, due to overlap with the negative peak regions, a weighted addition of the reference spectrum (i.e. the resting oxidation state of the analyte) was conducted to deconvolute a more accurate spectrum of the reduced species.

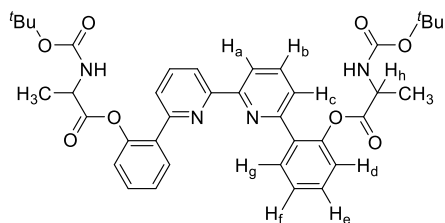
ii. *Synthesis*

6,6'-bis(Ph-2-acetate)-2,2'-bipyridine



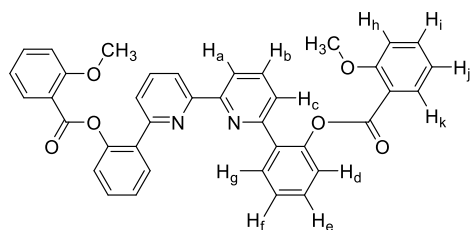
In a 100 mL 2-necked round-bottomed flask equipped with a reflux condenser, 6,6'-bis(2-hydroxyphenyl)-2,2'-bipyridine³ (0.29 mmol, 100 mg, 1.0 equiv.), dicyclohexylcarbodiimide (DCC) (0.87 mmol, 179 mg, 3.0 equiv.) and DMAP (0.06 mmol, 7 mg, 0.2 equiv.) were suspended in dry DCM. The flask was evacuated and backfilled with argon three times before acetic acid (0.87 mmol, 50 μ L, 3.0 equiv.) was added. The reaction mixture was continued to stir overnight. After 24 hours the resulting white precipitate was removed via vacuum filtration and the light-yellow solution diluted with DCM (10 mL) and subsequently washed with aqueous 0.1 M HCl (2 x 10 mL) and saturated aqueous NaHCO₃ (2 x 10 mL). The organic layer was then dried with MgSO₄ and purified via column chromatography (silica, DCM/MeOH 95:5) to give the product as a colorless solid (103 mg, 0.24 mmol, 84% yield). FTIR (CH₃CN): ν (C=O) 1768 cm⁻¹. LC-MS: m/z C₂₆H₂₁N₂O₄⁺ calc. 425.2 expt. 425.2. ¹H NMR (400 MHz, CDCl₃): δ (ppm) 8.51 (H_a dd, J = 7.9, 1.0 Hz, 2H), 7.89 (H_b dd, J = 7.9, 7.9 Hz, 2H), 7.81 (H_c dd, J = 7.5, 1.8 Hz, 2H), 7.57 (H_g dd, J = 7.6, 1.0 Hz, 2H), 7.47 (H_f ddd, J = 7.5, 7.5, 1.8 Hz, 2H), 7.41 (H_e ddd, J = 7.9, 7.9, 1.3 Hz, 2H), 7.22 (H_d dd, J = 7.9, 1.3 Hz, 2H), 2.14 (CH₃ s, 6H). ¹³C NMR (100 MHz, CDCl₃): δ (ppm) 169.8, 155.8, 155.2, 148.4, 137.5, 133.4, 131.2, 129.8, 126.6, 123.8, 123.6, 119.7, 21.3.

6,6'-bis(2-Boc-ala-Ph)-2,2'-bipyridine



An identical procedure was employed as per the 6,6'-bis(2-acetyl-Ph)-2,2'-bipyridine synthesis with the only exception being to add *N*-Boc-*L*-alanine (2.68 mmol, 507 mg, 4.0 equiv.) in place of acetic acid. The crude product was purified via column chromatography (silica, DCM/acetone 10:1) producing a white solid (129 mg, 0.19 mmol, 28% yield). FTIR (CH₃CN): $\nu(\text{C}=\text{O})$ 1772, 1713 cm⁻¹. LC-MS: m/z C₃₈H₄₃N₄O₈⁺ calc. 683.3 expt. 683.3. ¹H NMR (400 MHz, CDCl₃): δ (ppm) 8.46 – 8.49 (H_a m, 2H), 7.87 (H_b dd, $J = 7.9, 7.9$ Hz, 2H), 7.75 – 7.80 (H_c m, 2H), 7.52 – 7.55 (H_g m, 2H), 7.48 (H_f ddd, $J = 8.0, 8.0, 1.6$ Hz, 2H), 7.42 (H_e ddd, $J = 7.9, 7.9, 1.3$ Hz, 2H), 7.22 (H_d d, $J = 7.9$ Hz, 2H), 5.11 (NH(ala) m, 2H), 4.41 (H_h m, 2H), 1.42 (tBu(boc) s, 18H), 1.26 (CH₃(ala) s, 6H). ¹³C NMR (100 MHz, CDCl₃): δ (ppm) 172.0, 155.7, 155.1, 155.0, 148.1, 137.4, 133.8, 131.2, 129.9, 126.7, 124.2, 123.2, 119.9, 80.1, 49.5, 28.5, 18.3.

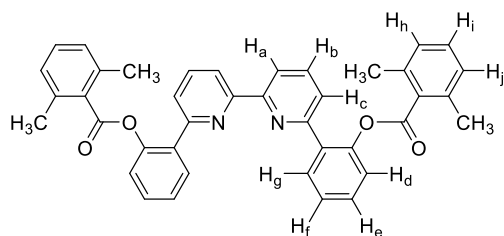
6,6'-bis(2-methoxybenzoate-Ph)-2,2'-bipyridine



An identical procedure was employed as per the 6,6'-bis(2-acetyl-Ph)-2,2'-bipyridine synthesis with the only exception being to add 2-methoxybenzoic acid (1.41 mmol, 215 mg, 4.0 equiv.) in place of acetic acid. The crude product was purified via column chromatography (silica, DCM/MeOH 95:5) to give the product as a yellow solid (134 mg, 0.22 mmol, 63%). FTIR

(CH₃CN): $\nu(\text{C}=\text{O})$ 1747 cm⁻¹. LC-MS: m/z C₃₈H₂₉N₂O₆⁺ calc. 609.2 expt. 609.1. ¹H NMR (400 MHz, CDCl₃): δ (ppm) 8.31 (H_a d, J = 8.0 Hz, 2H), 7.85 (H_b dd, J = 7.4, 1.6 Hz, 2H), 7.80 (H_c dd, J = 7.8, 1.6 Hz, 2H), 7.64 (H_i dd, J = 8.0, 8.0 Hz, 2H), 7.57 (H_g d, J = 7.6 Hz, 2H), 7.47 (H_f ddd, J = 8.0, 8.0, 2.0 Hz, 2H), 7.41 (H_e ddd, J = 7.9, 7.9, 1.2 Hz, 2H), 7.32 – 7.36 (H_d+H_k m, 4H), 6.85 (H_h d, J = 8.8, 2H), 7.64 (H_j dd, J = 7.6, 7.6, 2H), 3.77 (CH₃ s, 6H). ¹³C NMR (100 MHz, CDCl₃): δ (ppm) 164.1, 159.6, 155.3, 154.6, 148.3, 136.6, 133.9, 133.3, 132.1, 130.8, 129.4, 126.0, 123.6, 123.5, 119.7, 119.4, 118.7, 111.7, 55.7.

6,6'-bis(2,6-Me₂PhCO₂Ph)-2,2'-bipyridine



An identical procedure was employed as per the 6,6'-bis(2-acetyl-Ph)-2,2'-bipyridine synthesis with the only exception being to add 2,6-dimethylbenzoic acid (1.41 mmol, 212 mg, 4.0 equiv.) in place of acetic acid. The crude product was purified via column chromatography (silica, DCM/MeOH 95:5) to give the product as a yellow solid (74 mg, 0.14 mmol, 35%). FTIR (CH₃CN): $\nu(\text{C}=\text{O})$ 1747 cm⁻¹. LC-MS: m/z C₄₀H₃₃N₂O₄⁺ calc. 605.2 expt. 605.3. ¹H NMR (400 MHz, CDCl₃): δ (ppm) 8.42 (H_a d, J = 7.6 Hz, 2H), 7.94 (H_b dd, J = 8.0, 1.6 Hz, 2H), 7.72 (H_c dd, J = 8.0, 7.6 Hz, 2H), 7.62 (H_g dd, J = 7.6 Hz, 2H), 7.55 (H_f ddd, J = 8.0, 8.0, 1.6 Hz, 2H), 7.47 (H_e dd, J = 7.6, 1.2 Hz, 2H), 7.39 (H_i d, J = 8.0 Hz, 2H), 7.19 (H_d d, J = 8.0 Hz, 2H), 7.00 (H_h+H_j d, J = 7.6 Hz, 4H), 2.19 (s, 12H). ¹³C NMR (100 MHz, CDCl₃): δ (ppm) 155.9, 154.6, 139.6, 136.9, 135.6, 134.1, 131.5, 129.8, 129.7, 127.8, 126.5, 124.4, 123.0, 119.9, 119.8, 19.8.

General procedure for [*fac*-Mn^I(OTf)(R₂bpy)(CO)₃] complex synthesis

Following a reported procedure for the synthesis of *fac*-Mn(CO)₅(OTf),⁴ bromopentacarbonylmanganese(I) (50 mg, 0.18 mmol) was added to 20 ml of dichloromethane in a 50 ml round bottom flask under 1 atm argon. Silver triflate (46 mg, 0.18 mmol) was added and the reaction mixture was allowed to stir in the dark. After one hour, the reaction mixture was filtered through a celite plug by vacuum filtration to remove the resulting AgBr precipitate. The filtrate was dried by rotary evaporation, quantitatively yielding *fac*-Mn(CO)₅(OTf) as a yellow solid. This intermediate was dissolved in 3 ml of THF in a 10 ml microwave reaction tube and 0.9 equivalents of ligand (0.16 mmol) was added under argon. The reaction tube was sealed and irradiated at 100 W in the microwave at 80°C for 15 min. Upon completion and cooling to room temperature, the volume of THF was reduced under vacuum to approximately 0.5 ml, then 10 ml of diethyl ether was added to yield a fine yellow precipitate which was collected by vacuum filtration. All solids were washed with cold diethyl ether and dried under vacuum overnight in a sealed round bottom flask.

[1-OTf] [Mn(OTf)((Ph-2-acetate)₂bpy)(CO)₃]

Product yield: 38 mg (0.05 mmol, 33%). FTIR (CH₃CN): $\nu(\text{C}\equiv\text{O})$ 2043, 1958, 1949, $\nu(\text{C}=\text{O})$ 1768 cm⁻¹. HRMS: m/z C₃₁H₂₃MnN₃O₇⁺ calc. 604.09110 expt. 604.09031 (3.5%). ¹H NMR (400 MHz, CD₃CN): δ (ppm) 8.51 (t, J = Hz, 2H), 8.24 (t, J = Hz, 2H), 7.66 – 7.44 (m, 8H), 7.35 – 7.31 (m, 2H), 2.03 – 1.95 (m, 6H).

[2-OTf] [Mn(OTf)((PhO(2-Boc-ala-Ph)₂bpy)(CO)₃]

Product yield: 132 mg (0.14 mmol, 85%). FTIR (CH₃CN): $\nu(\text{C}\equiv\text{O})$ 2043, 1957, $\nu(\text{C}=\text{O})$ 1772, 1713 cm⁻¹. HRMS: m/z C₄₃H₄₅MnN₅O₁₁⁺ calc. 862.24906 expt. 862.24103 (19%). ¹H NMR (400 MHz, CD₃CN): δ (ppm) 8.46 (s, 2H), 8.17 (s, 2H), 7.61 – 7.22 (m, 10H), 5.70 – 5.47 (m, 2H), 4.15 – 3.93 (m, 2H), 1.34 – 0.75 (m, 24H).

[3-OTf] [Mn(OTf)((2-methoxybenzoate-Ph)₂bpy)(CO)₃]

Product yield: 30 mg (0.03 mmol, 21% yield). FTIR (CH₃CN): $\nu(\text{C}\equiv\text{O})$ 2043, 1957, $\nu(\text{C}=\text{O})$ 1747, 1729 cm⁻¹. HRMS m/z calcd. C₄₃H₃₁MnN₃O₉⁺ 788.14353 expt. 788.14245. ¹H NMR (400 MHz, CD₃CN): δ (ppm) 8.38 (m, 4H), 8.14 (m, 6H), 7.70-7.40 (m, 8H), 6.88 (m, 4H), 3.65 (s, 6H).

[4-OTf] [Mn(OTf)((Me₂PhCO₂Ph)₂bpy)(CO)₃]

Product yield: 28 mg (0.03 mmol, 20%). FTIR (CH₃CN): $\nu(\text{C}\equiv\text{O})$ 2044, 1958, 1948(sh), $\nu(\text{C}=\text{O})$ 1769, 1755(sh) cm⁻¹. HRMS: m/z C₄₅H₃₅MnN₃O₇⁺ calc. 784.18554 expt. 784.18554 (3.5%). ¹H NMR (400 MHz, CD₃CN): δ (ppm) 8.33 (m, 2H), 7.84 (m, 4H), 7.61 (m, 4H), 7.51 (m, 2H), 7.44 (m, 2H), 7.22 (m, 2H), 7.03 (m, 4H), 2.09 (m, 12H).

2. Computational Methods

All geometries were fully optimized at the MN15 level of density functional theory⁵ in conjunction with the SMD continuum solvation model⁶ for acetonitrile using def2-TZVP basis set⁷ on Mn and the def2-SVP basis set on all other atoms. Non-analytical integrals were evaluated using the integral=(grid=ultrafine) option as implemented in the Gaussian 16 software package.⁸ The nature of all stationary points was verified by analytic computation of vibrational frequencies, which were also used for the computation of zero-point vibrational energies, molecular partition functions, and for determining the reactants and products associated with each transition-state structure by following the normal modes associated with imaginary frequencies. Partition functions were used in the computation of 298 K thermal contributions to the free energy employing the usual ideal-gas, rigid-rotator, harmonic oscillator approximation.⁹ To avoid spurious errors for the free energy calculations, all frequencies below 50 cm⁻¹, except the imaginary frequency of transition states, were replaced by 50 cm⁻¹. For computational efficiency the terminal tert-butyl substituents of the N-boc protecting groups were modeled as methyl groups. Free-energy contributions were added to single-point MN15 electronic energies computed using SMD continuum solvation model for acetonitrile at the optimized geometries obtained with the initial basis with the def2-TZVP basis set on all atoms to arrive at final composite free energies.

3. High-resolution mass spectrometry data

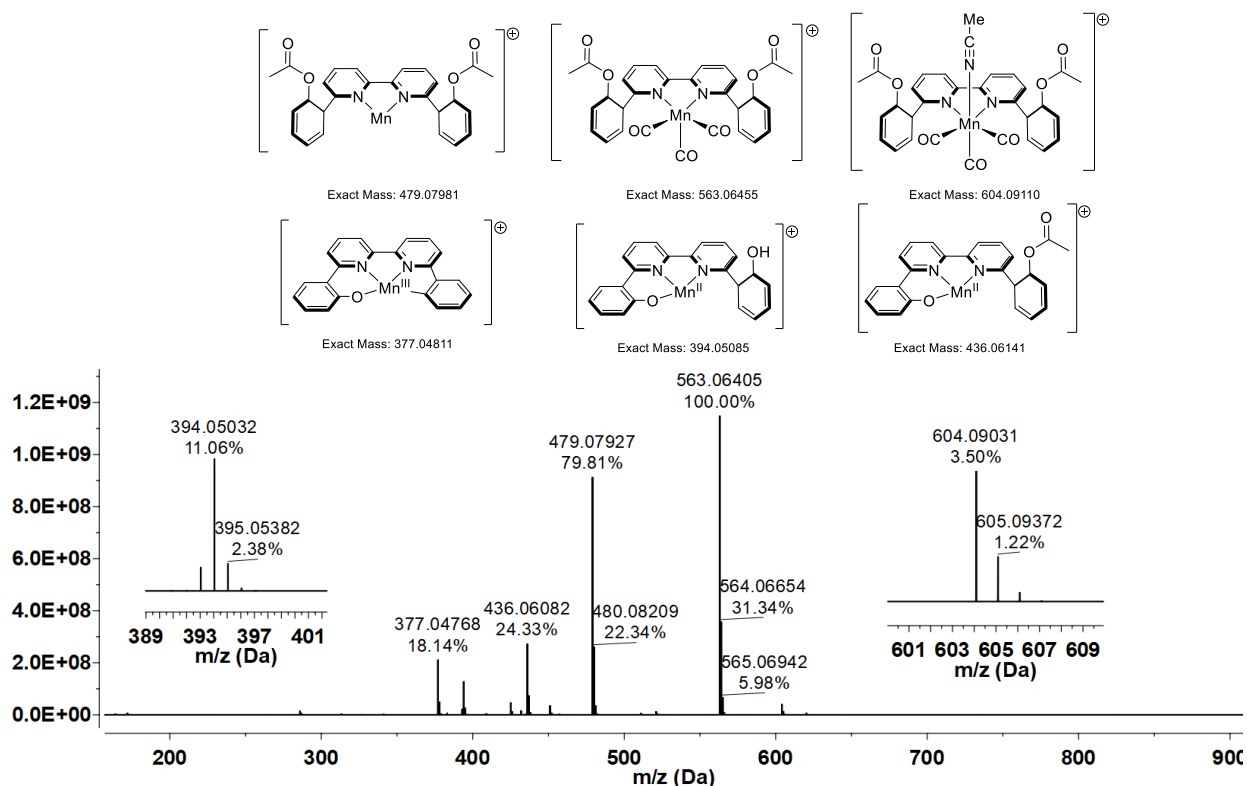


Figure ESI-1. HRMS (MeCN) at 2.6 KeV of complex [1-CH₃CN]⁺. Peak assignments are provided with molecular structures.

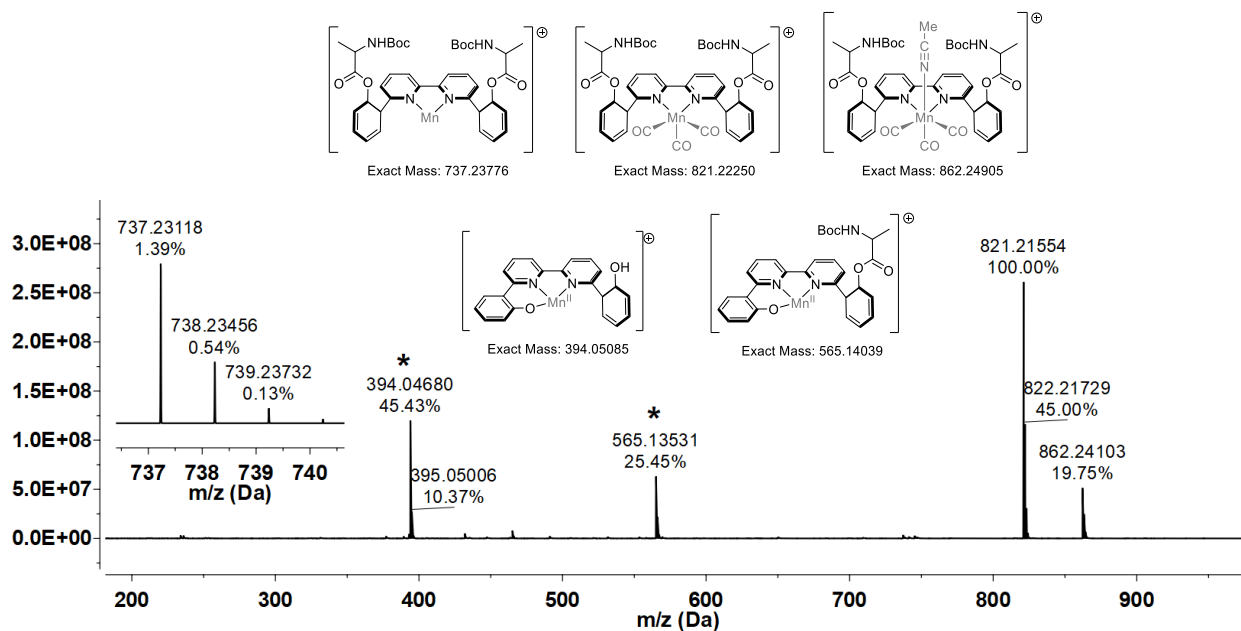


Figure ESI-2. HRMS (MeCN) at 2.6 KeV of complex [2-CH₃CN]⁺. Peak assignments are provided with molecular structures.

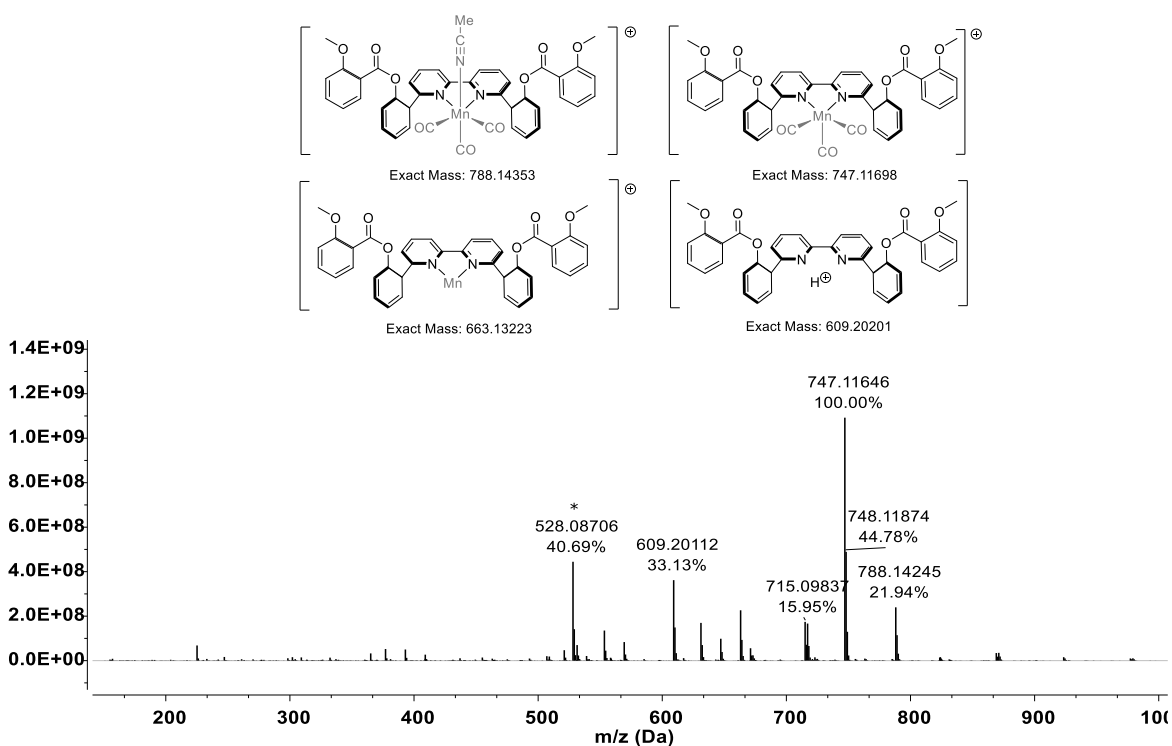


Figure ESI-3. HRMS (MeCN) at 2.6 KeV of complex $[3\text{-CH}_3\text{CN}]^+$. Peak assignments are provided with molecular structures.

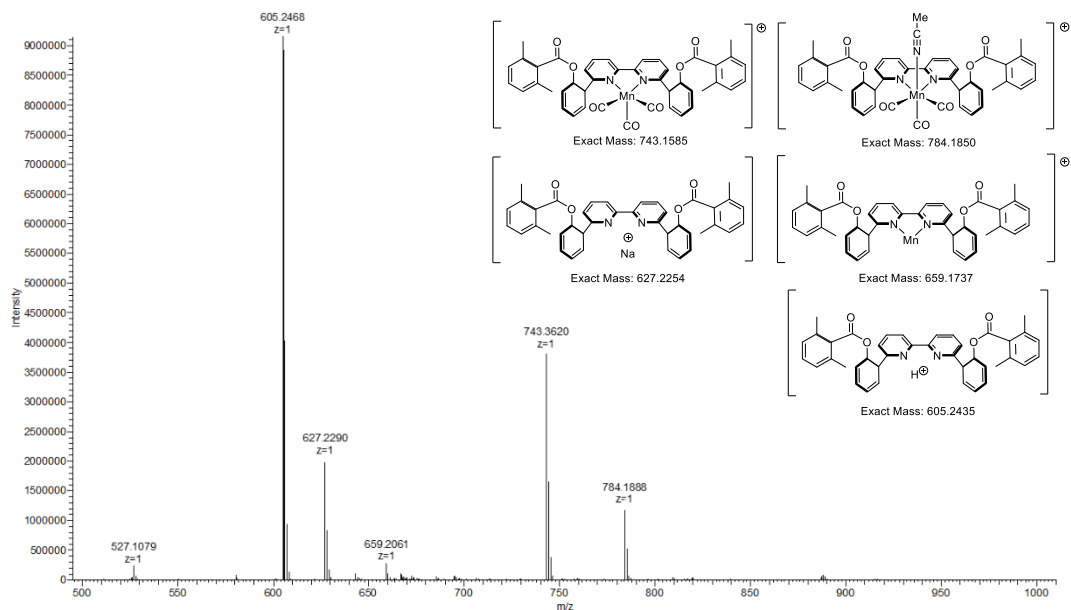


Figure ESI-4. HRMS (MeCN) at 2.6 KeV of complex $[4\text{-CH}_3\text{CN}]^+$. Peak assignments are provided with molecular structures.

4. NMR spectrometry data

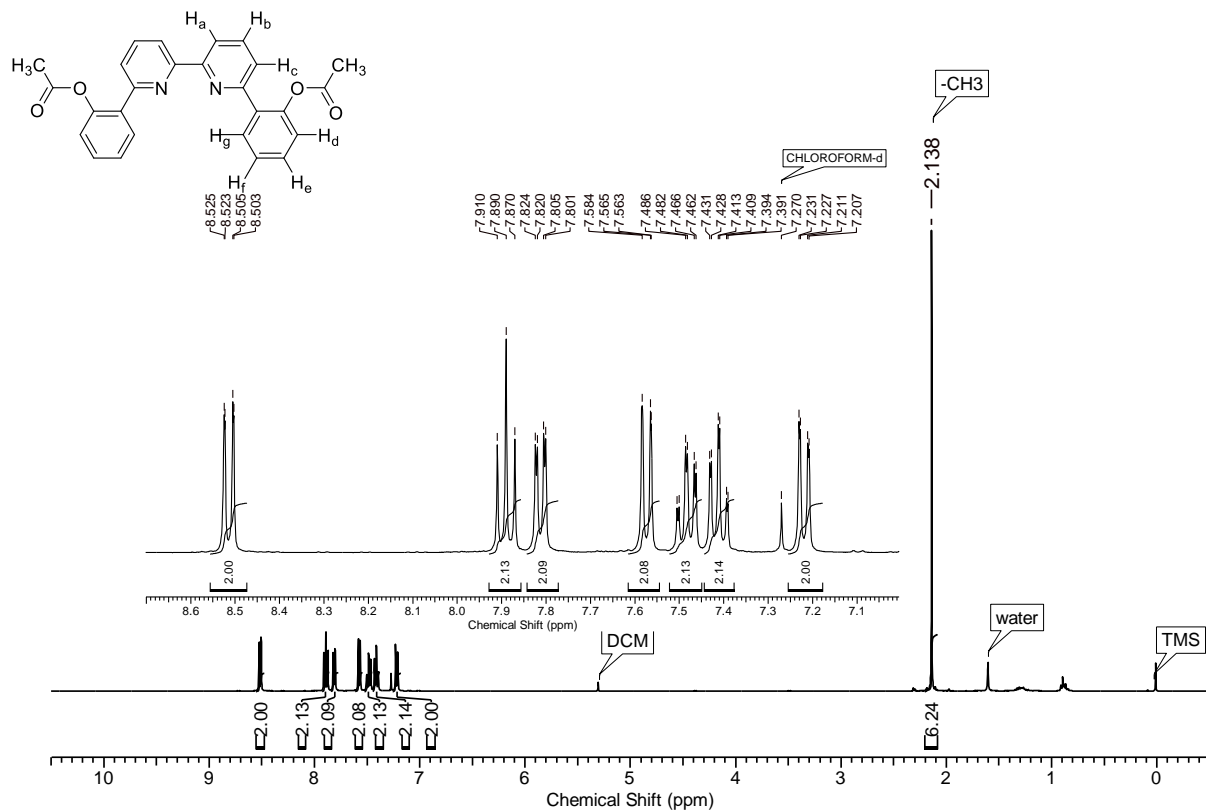


Figure ESI-5. 1H NMR spectrum of 6,6'-bis(Ph-2-acetate)-2,2'-bipyridine recorded in CDCl₃.

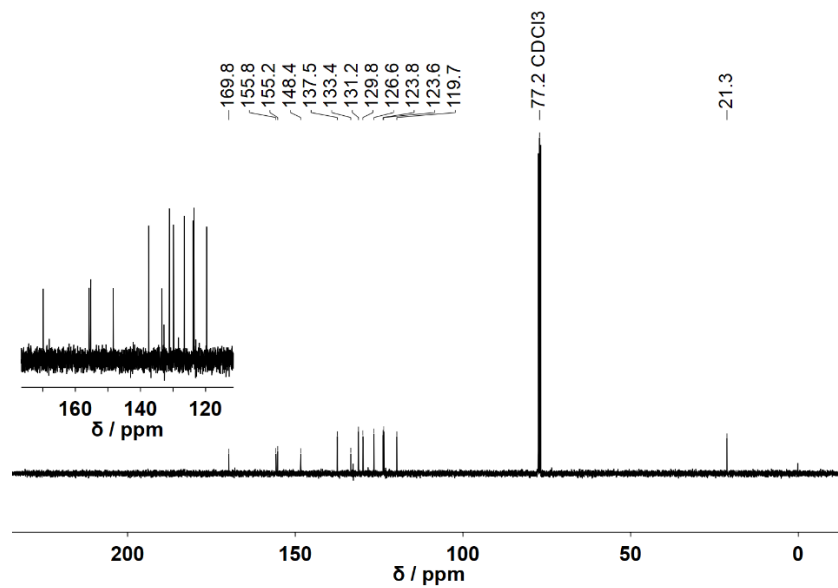


Figure ESI-6. ^{13}C NMR spectrum of 6,6'-bis(Ph-2-acetate)-2,2'-bipyridine recorded in CDCl₃.

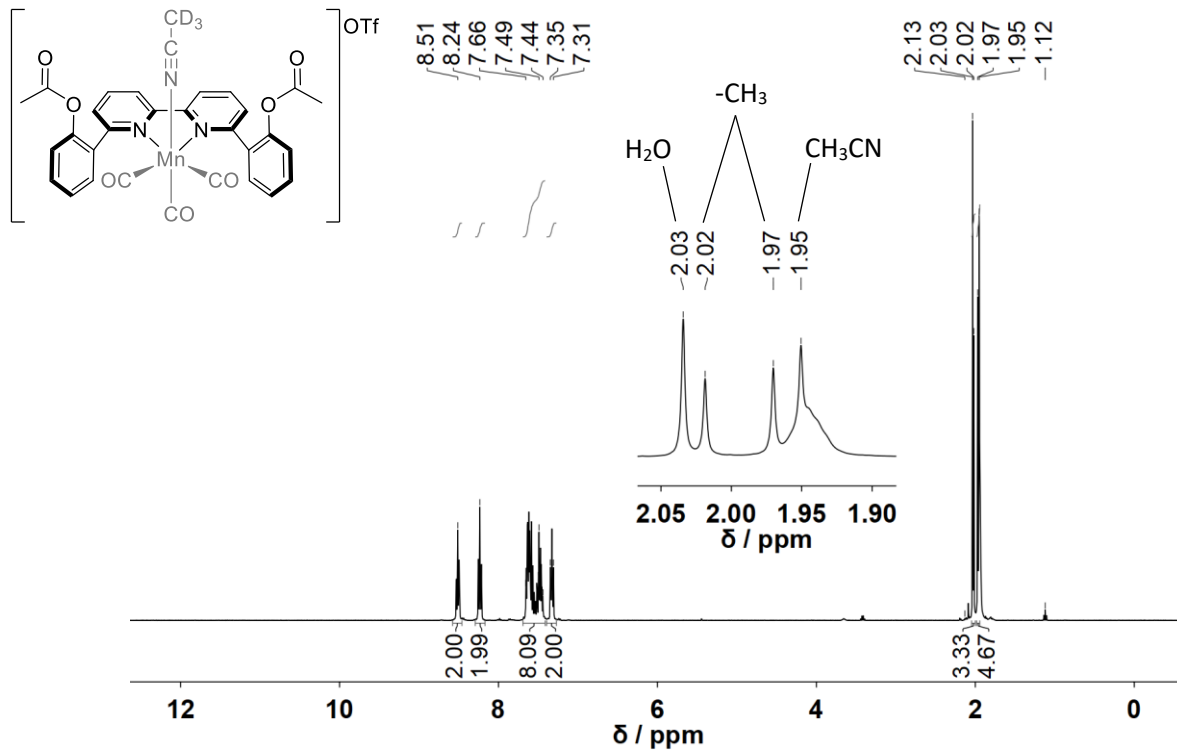


Figure ESI-7. ^1H NMR spectrum of $[\text{1-CD}_3\text{CN}]^+$ recorded in CD₃CN.

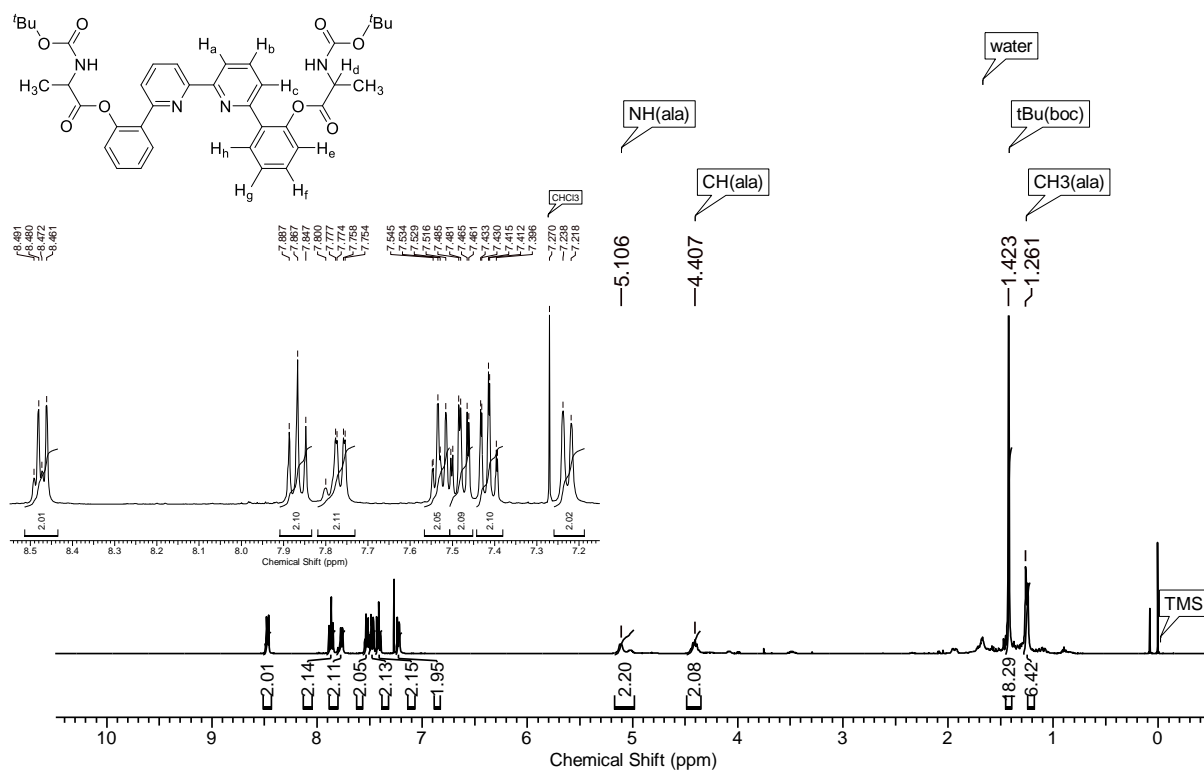


Figure ESI-8. ^1H NMR spectrum of 6,6'-bis(2-Boc-ala-Ph)-2,2'-bipyridine recorded in CDCl₃.

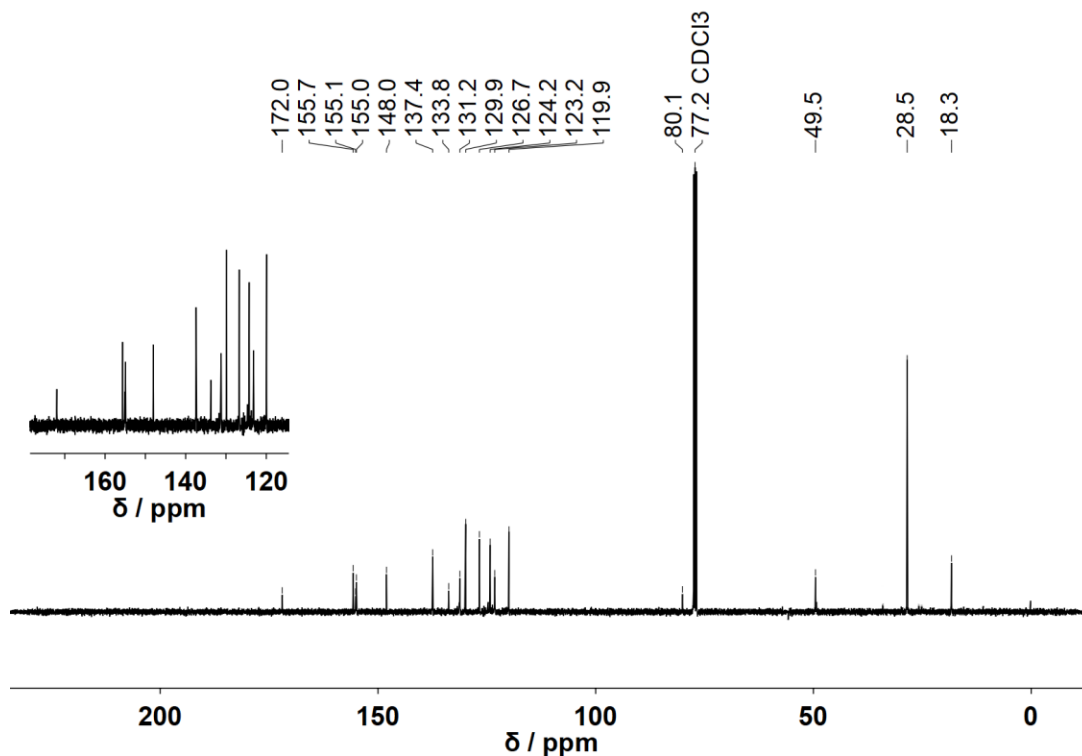


Figure ESI-9. ¹³C NMR spectrum of 6,6'-bis(2-Boc-ala-Ph)-2,2'-bipyridine recorded in CDCl₃.

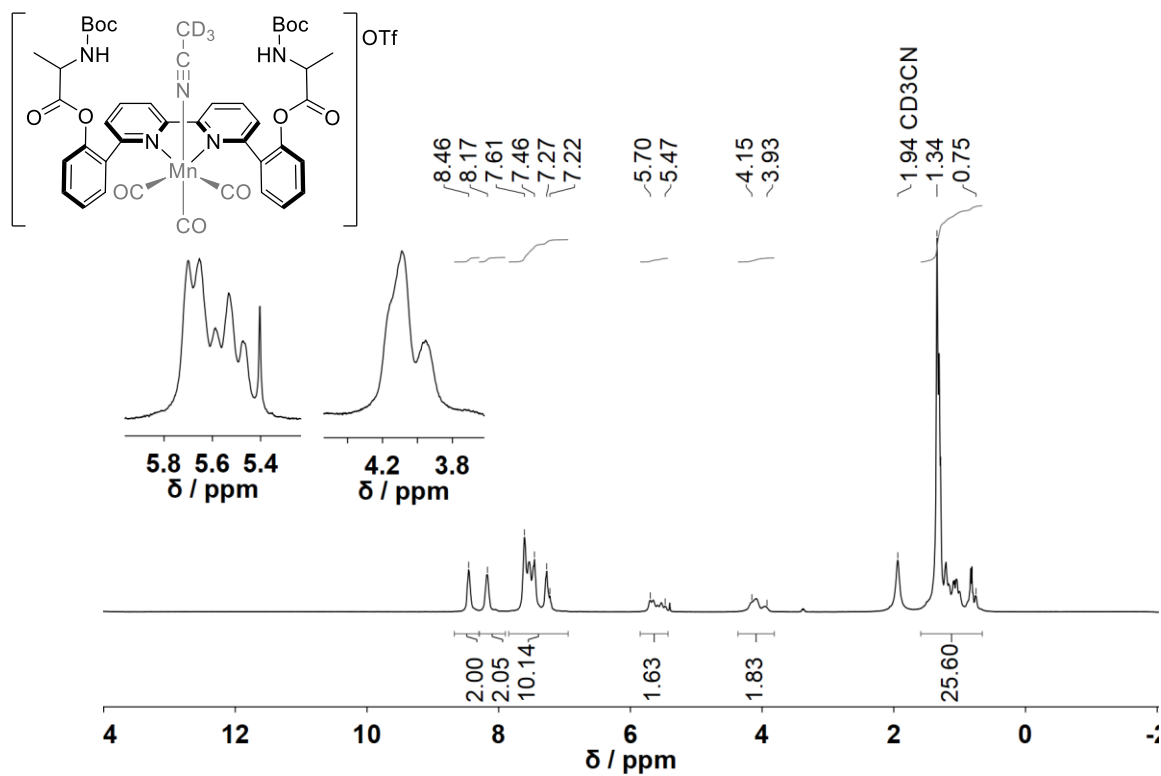


Figure ESI-10. ¹H NMR spectrum of [2-CD₃CN]⁺ recorded in CD₃CN.

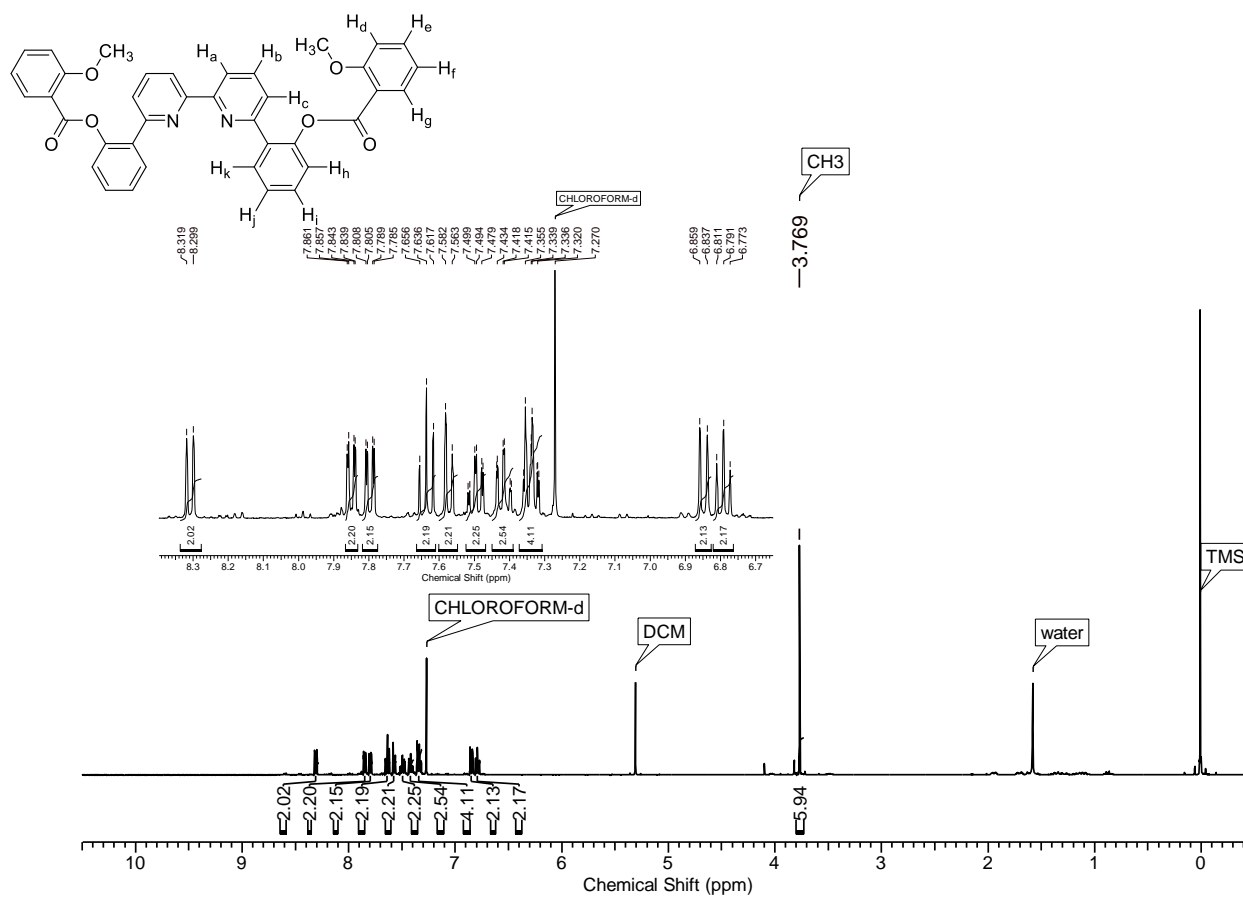


Figure ESI-11. ¹H NMR of 6,6'-bis(2-methoxybenzoate-Ph)-2,2'-bipyridine recorded in CDCl₃.

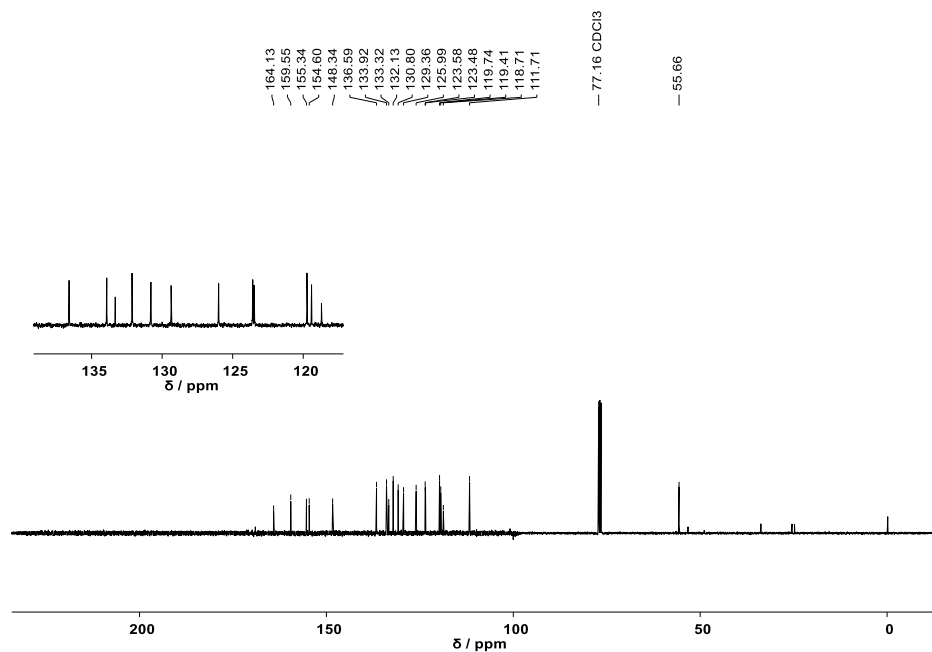


Figure ESI-12. ¹³C NMR of 6,6'-bis(2-methoxybenzoate-Ph)-2,2'-bipyridine recorded in CDCl₃.

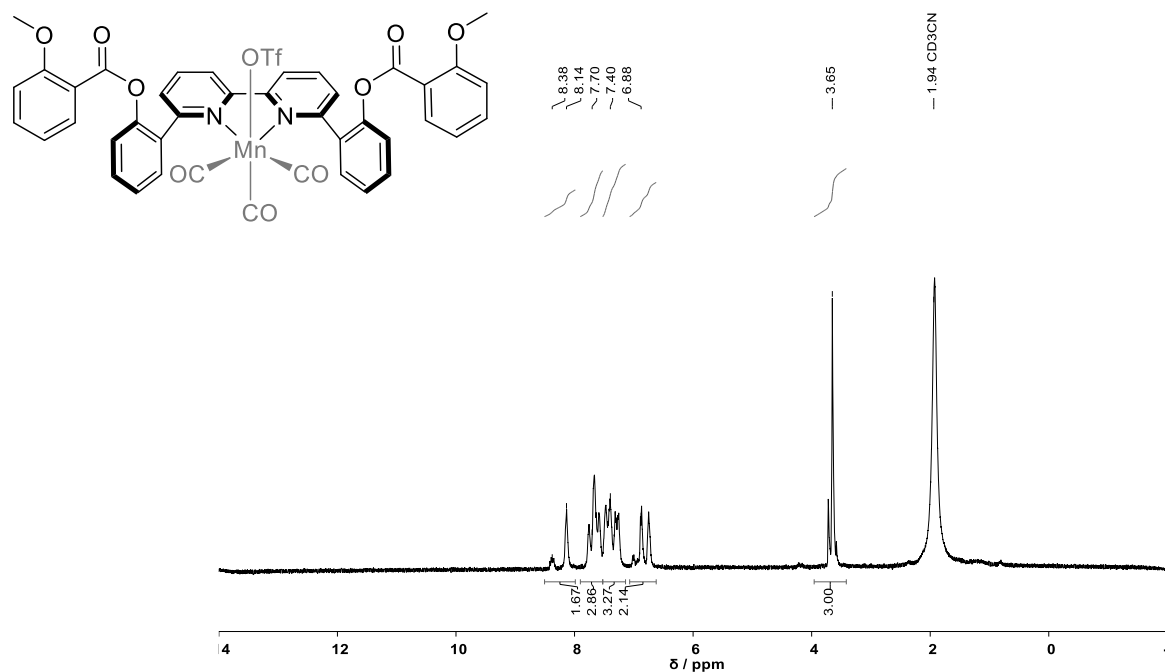


Figure ESI-13. ^1H NMR spectrum of $[\mathbf{3}\text{-CD}_3\text{CN}]^+$ recorded in CD_3CN .

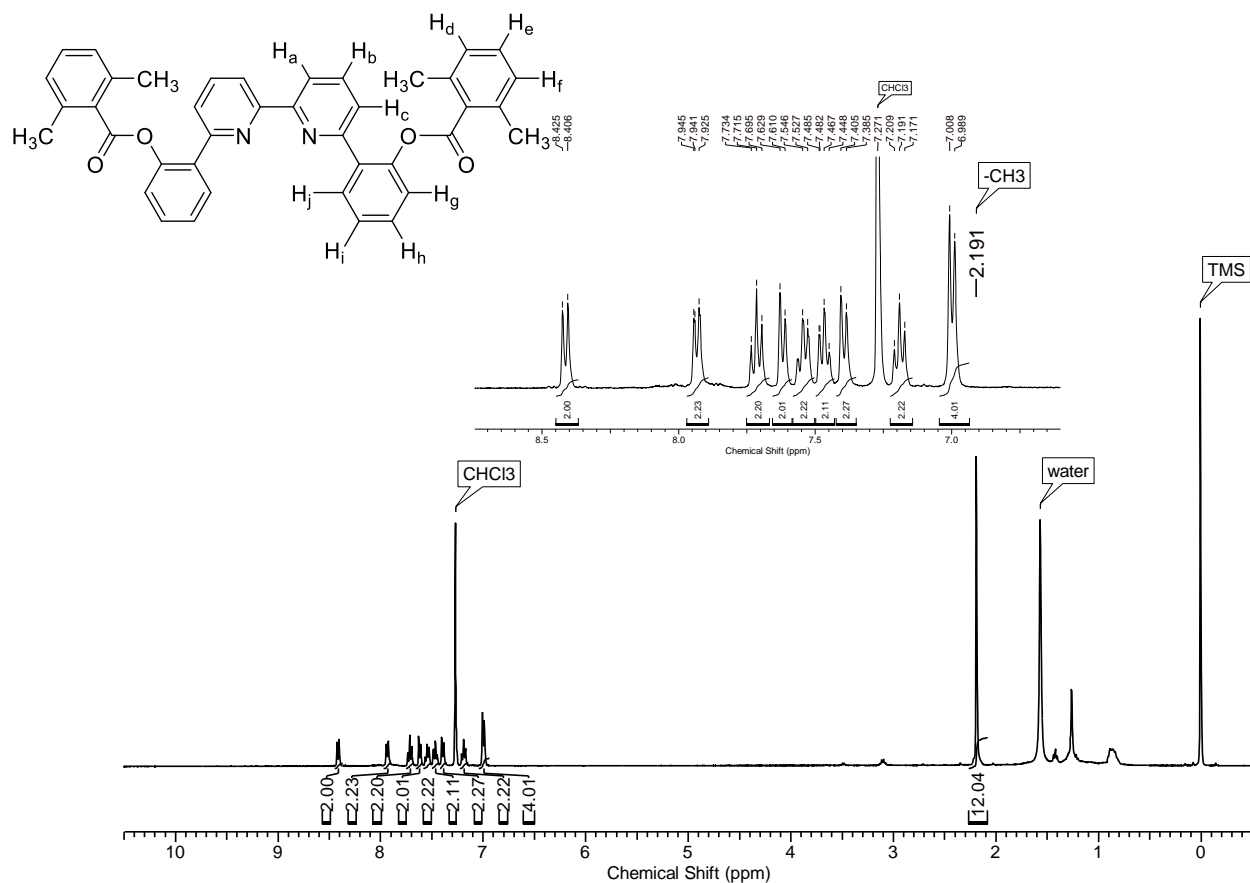


Figure ESI-14. ^1H NMR of 6,6'-bis(2,6-Me₂PhCO₂Ph)-2,2'-bipyridine recorded in CDCl_3 .

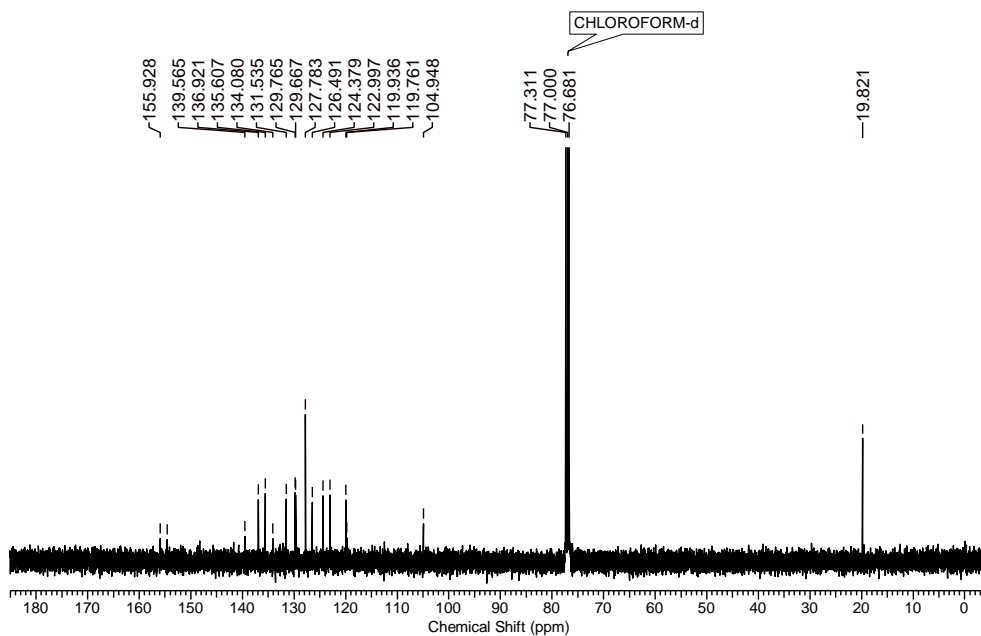


Figure ESI-15. ^{13}C NMR of 6,6'-bis(2,6-Me₂PhCO₂Ph)-2,2'-bipyridine recorded in CDCl₃.

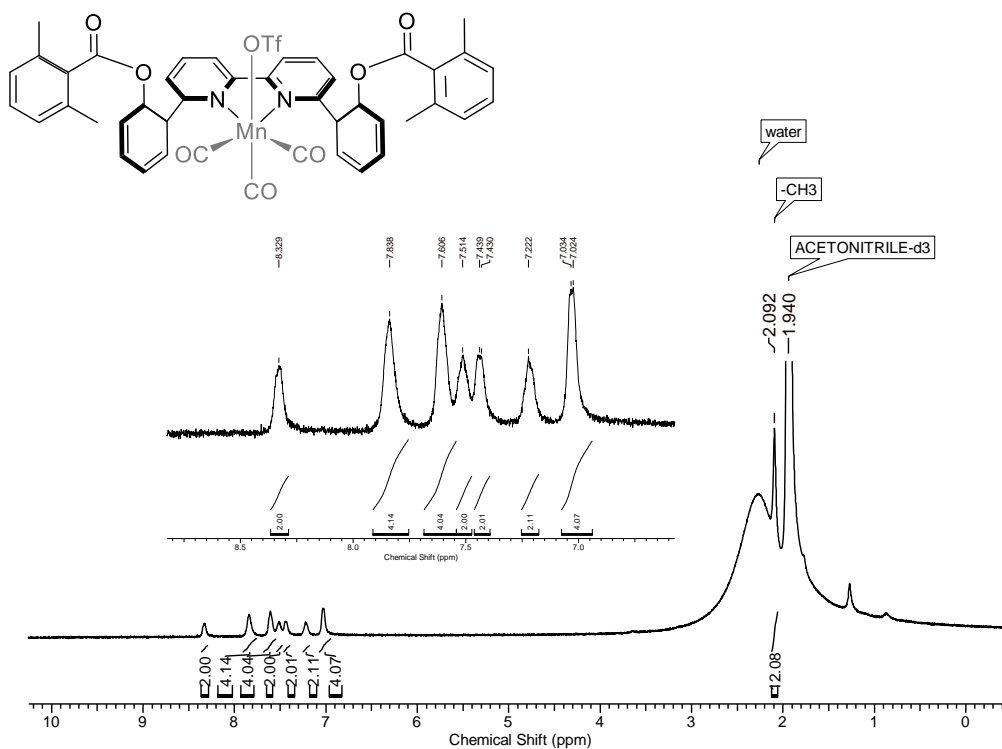


Figure ESI-16. ^1H NMR spectrum of [4-CD₃CN]⁺ recorded in CD₃CN.

5. Cyclic voltammetry under 1 atm argon

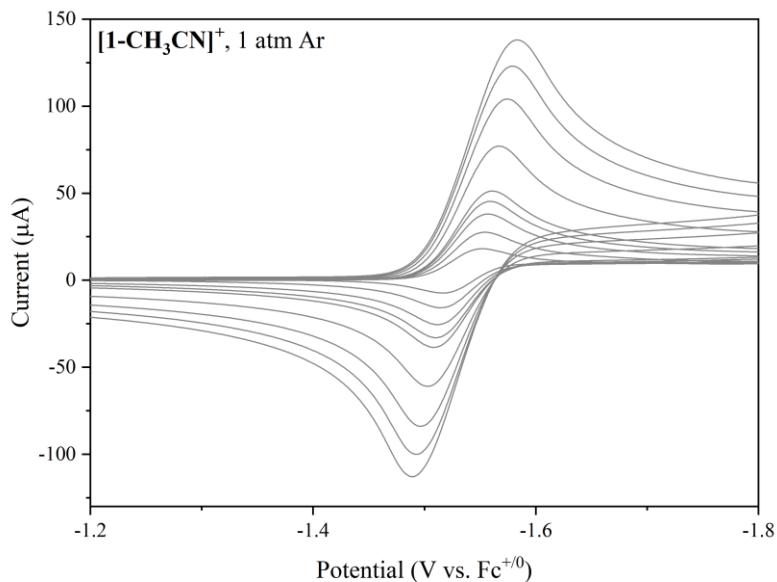


Figure ESI-17. Scan rate dependent cyclic voltammetry data for the first reduction of $[1-CH_3CN]^+$ recorded under 1 atm of argon in 0.1 M $[Bu_4N][PF_6]$ acetonitrile supporting electrolyte. CVs were recorded at scan rates of 0.01, 0.025, 0.05, 0.075, 0.1, 0.25, 0.5, 0.75, and 1.0 $V s^{-1}$.

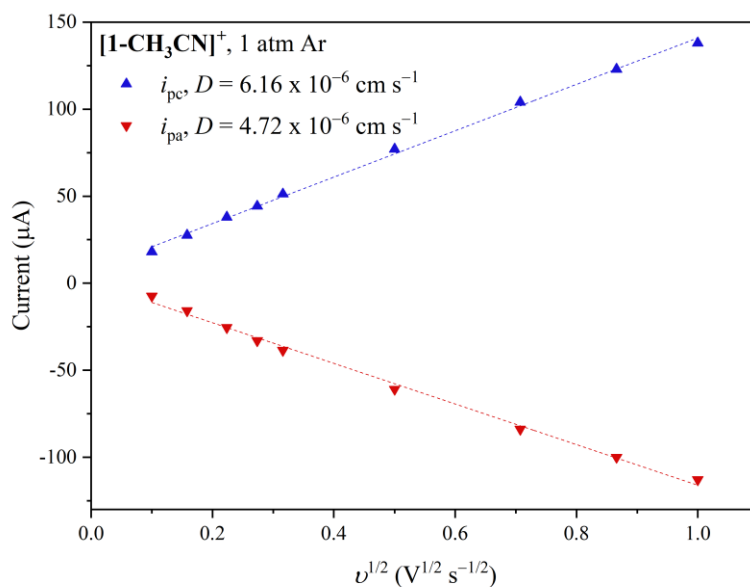


Figure ESI-18. Randles-Sevcik plot for the first reduction of $[1-CH_3CN]^+$ recorded at 1 mM concentration in 0.1 M $[Bu_4N][PF_6]$ acetonitrile supporting electrolyte under 1 atm of argon.

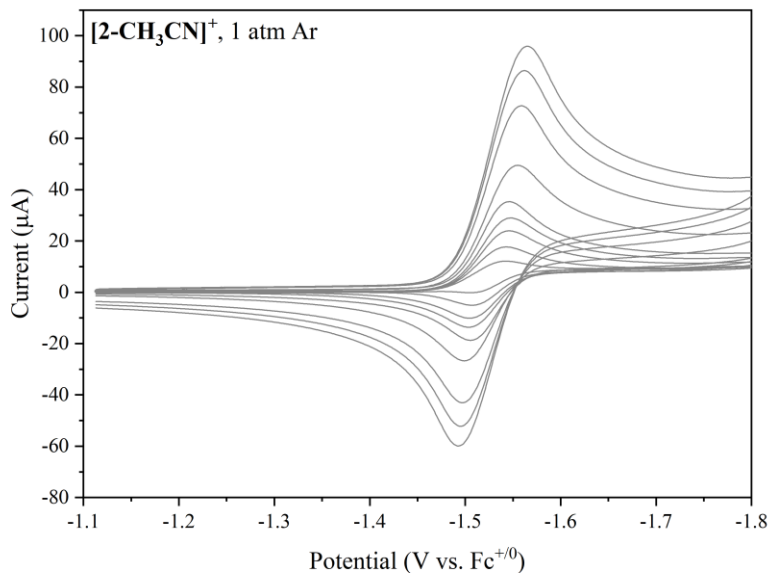


Figure ESI-19. Scan rate dependent cyclic voltammetry data for the first reduction of $[2\text{-CH}_3\text{CN}]^+$ recorded under 1 atm of argon in 0.1 M $[\text{Bu}_4\text{N}][\text{PF}_6]$ acetonitrile supporting electrolyte. CVs were recorded at scan rates of 0.01, 0.025, 0.05, 0.075, 0.1, 0.25, 0.5, 0.75, and 1.0 V s^{-1} .

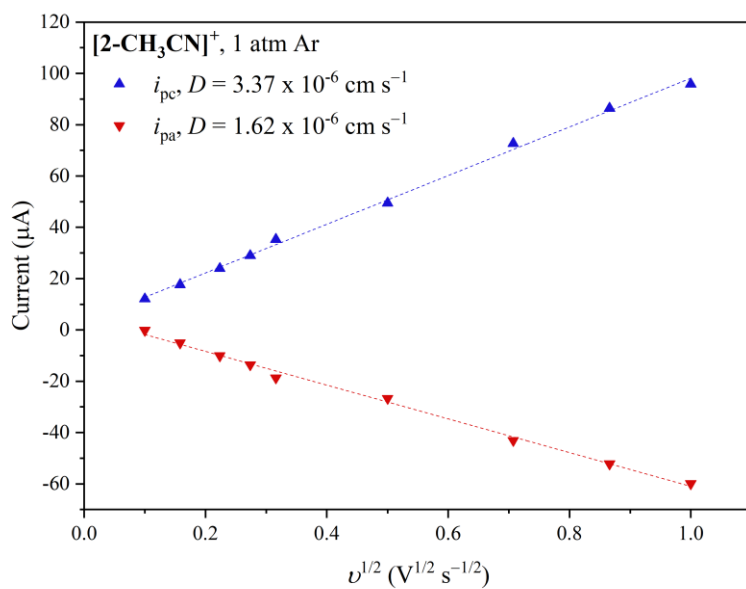


Figure ESI-20. Randles-Sevcik plot for the first reduction of $[2\text{-CH}_3\text{CN}]^+$ recorded at 1 mM concentration in 0.1 M $[\text{Bu}_4\text{N}][\text{PF}_6]$ acetonitrile supporting electrolyte under 1 atm of argon.

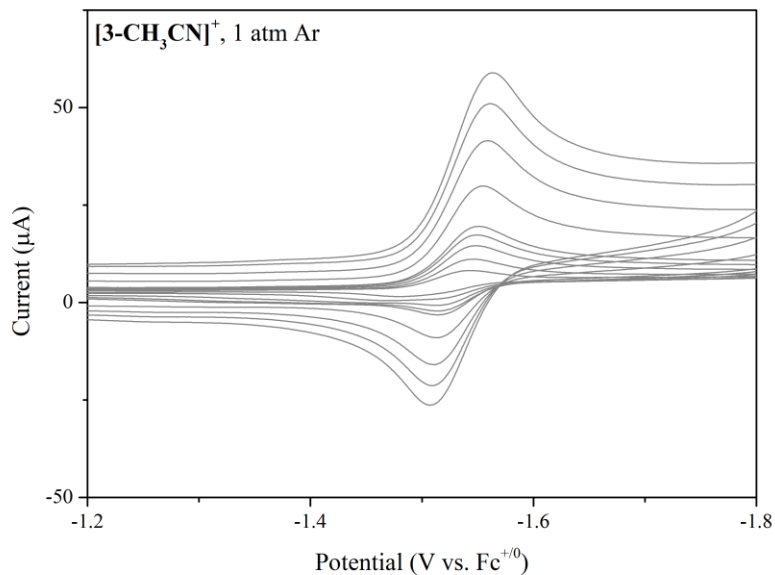


Figure ESI-21. Scan rate dependent cyclic voltammetry data for the first reduction of $[3\text{-CH}_3\text{CN}]^+$ recorded under 1 atm of argon in 0.1 M $[\text{Bu}_4\text{N}][\text{PF}_6]$ acetonitrile supporting electrolyte. CVs were recorded at scan rates of 0.01, 0.025, 0.05, 0.075, 0.1, 0.25, 0.5, 0.75, and 1.0 V s^{-1} .

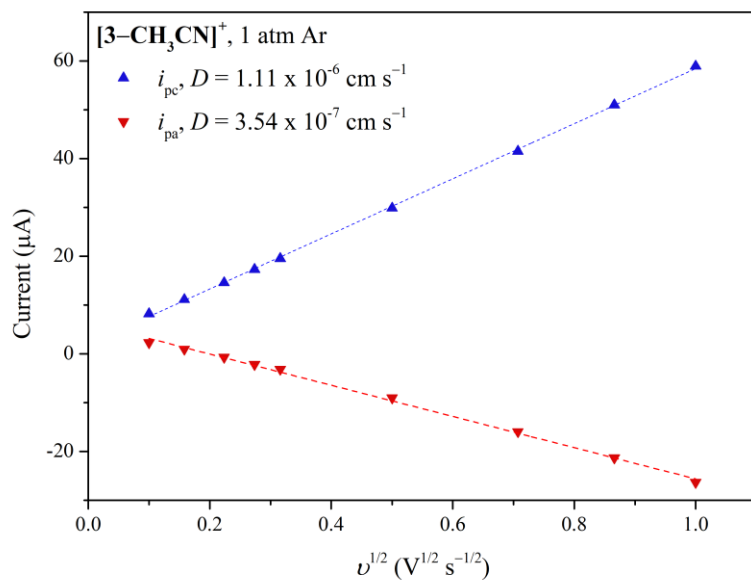


Figure ESI-22. Randles-Sevcik plot for the first reduction of $[3\text{-CH}_3\text{CN}]^+$ recorded at 1 mM concentration in 0.1 M $[\text{Bu}_4\text{N}][\text{PF}_6]$ acetonitrile supporting electrolyte under 1 atm of argon.

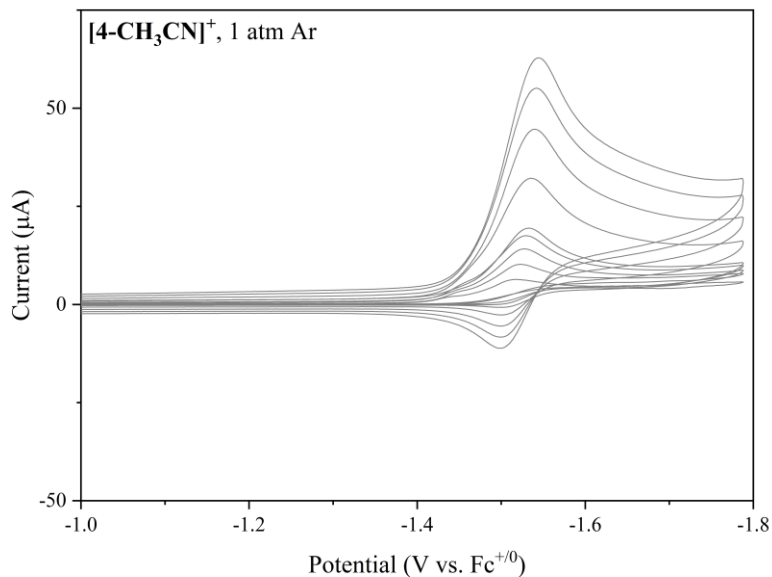


Figure ESI-23. Scan rate dependent cyclic voltammetry data for the first reduction of $[4\text{-CH}_3\text{CN}]^+$ recorded under 1 atm of argon in 0.1 M $[\text{Bu}_4\text{N}][\text{PF}_6]$ acetonitrile supporting electrolyte. CVs were recorded at scan rates of 0.01, 0.025, 0.05, 0.075, 0.1, 0.25, 0.5, 0.75, and 1.0 V s^{-1} .

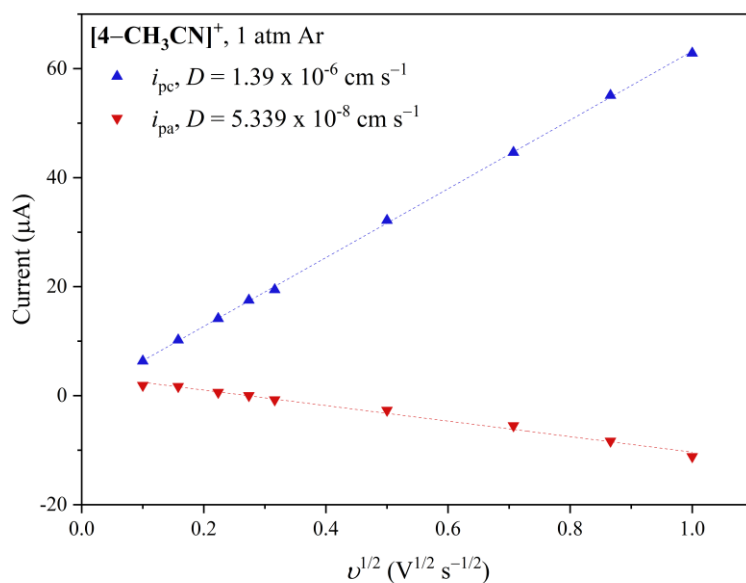


Figure ESI-24. Randles-Sevcik plot for the first reduction of $[4\text{-CH}_3\text{CN}]^+$ recorded at 1 mM concentration in 0.1 M $[\text{Bu}_4\text{N}][\text{PF}_6]$ acetonitrile supporting electrolyte under 1 atm of argon.

6. Infrared spectroelectrochemistry

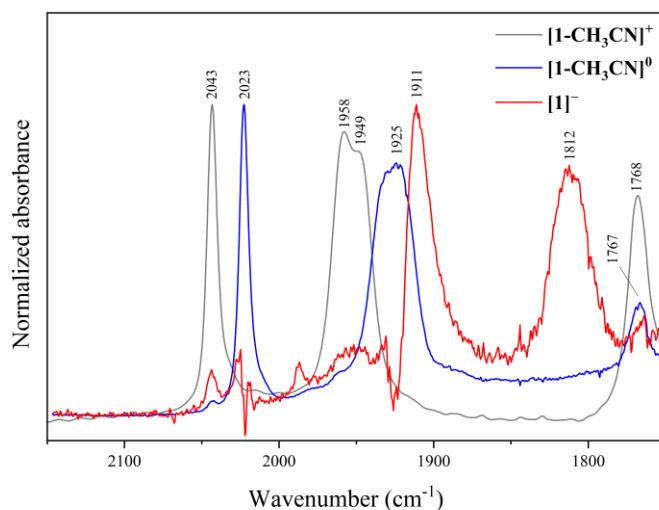


Figure ESI-25. IRSEC spectral results upon electrolysis of $[1\text{-CH}_3\text{CN}]^+$ recorded in argon-saturated 0.1 M $[\text{Bu}_4\text{N}][\text{PF}_6]$ acetonitrile supporting electrolyte.

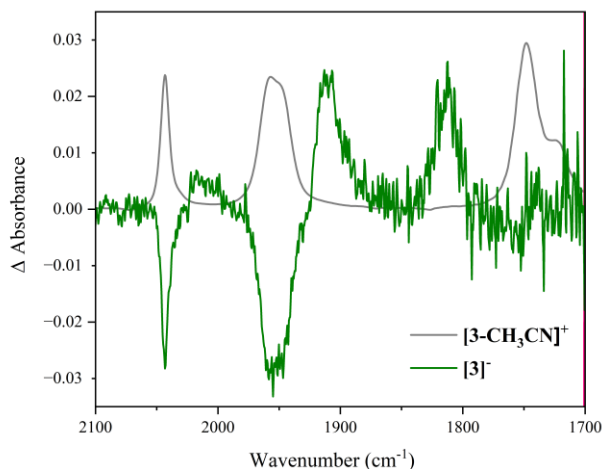


Figure ESI-26. IRSEC spectral results upon electrolysis of $[3\text{-CH}_3\text{CN}]^+$ recorded in argon-saturated 0.1 M $[\text{Bu}_4\text{N}][\text{PF}_6]$ acetonitrile supporting electrolyte. The one-electron reduced species $[3\text{-CH}_3\text{CN}]^0$, typically generated at very low concentrations is not observed due to poor solubility. This is further evident in the poor signal to noise upon quantitative reduction to the two-electron reduced $[3]^-$ anion.

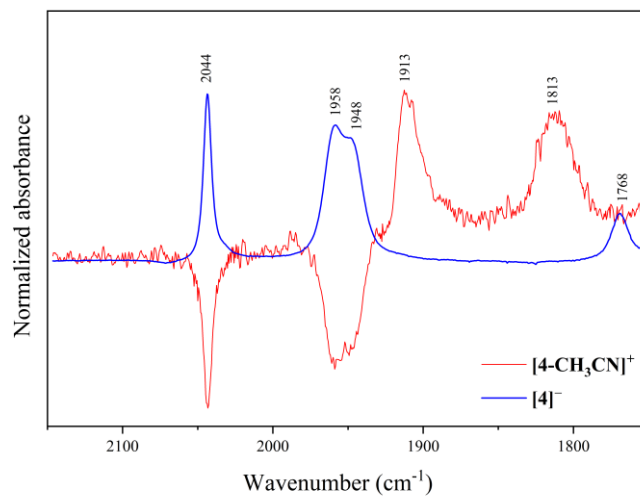


Figure ESI-27. IRSEC spectral results upon electrolysis of [4-CH₃CN]⁺ recorded in argon-saturated 0.1 M [Bu₄N][PF₆] acetonitrile supporting electrolyte. The one-electron reduced species [4-CH₃CN]⁰, typically generated at very low concentrations is not observed due to poor solubility. This is further evident in the poor signal to noise upon quantitative reduction to the two-electron reduced [4]⁻ anion.

7. Voltammetry under 1 atm CO₂

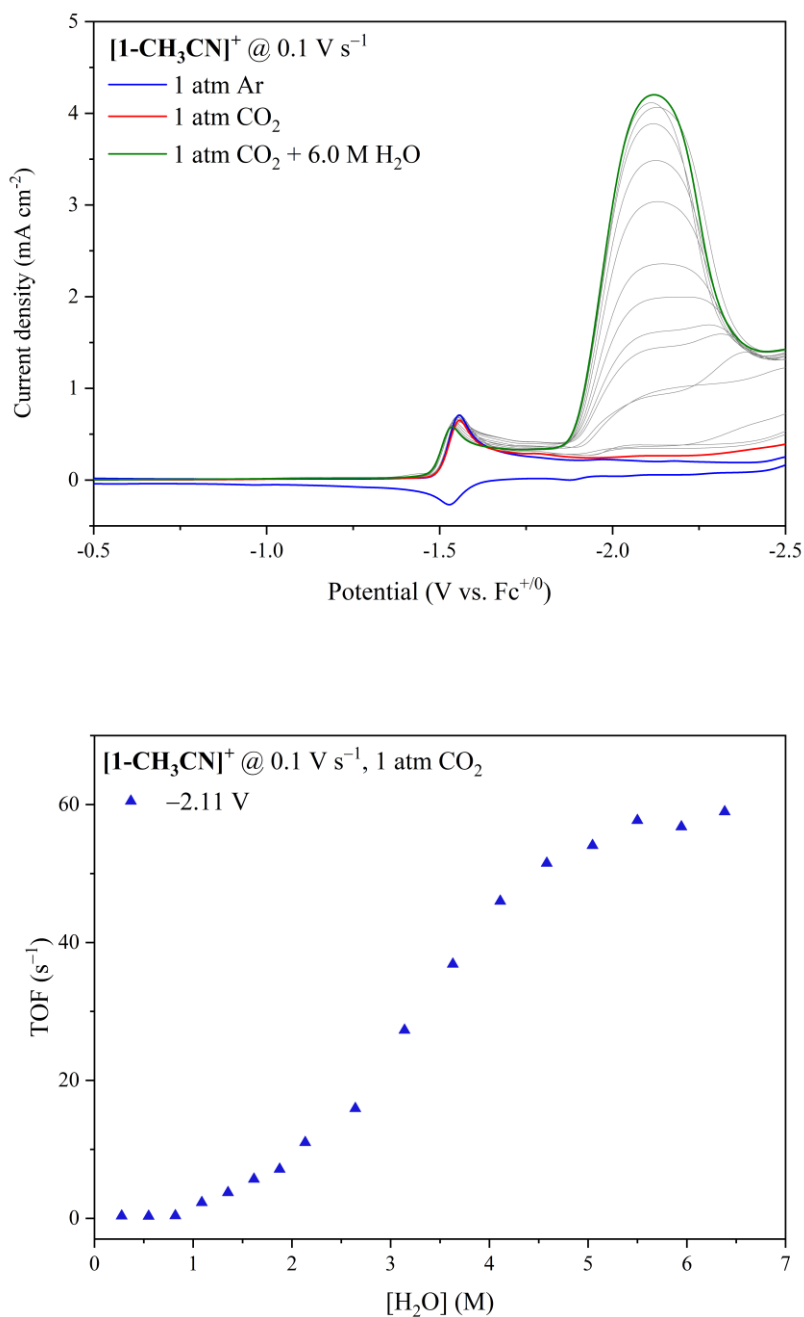


Figure ESI-28. (top) Linear sweep voltammetry of [1-CH₃CN]⁺ recorded at 1 mM catalyst concentration in 0.1 M [Bu₄N][PF₆] acetonitrile supporting electrolyte at a glassy carbon disc electrode with a scan rate (ν) of 0.1 V s⁻¹ under 1 atm CO₂ with increasing H₂O concentration. (bottom) Scatter plot of TOF vs [H₂O] determined at high overpotential (-2.11 V).

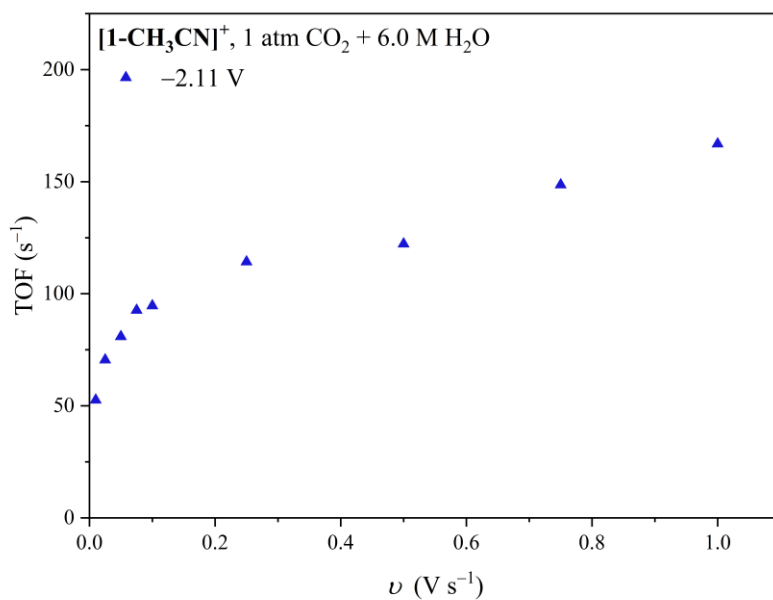
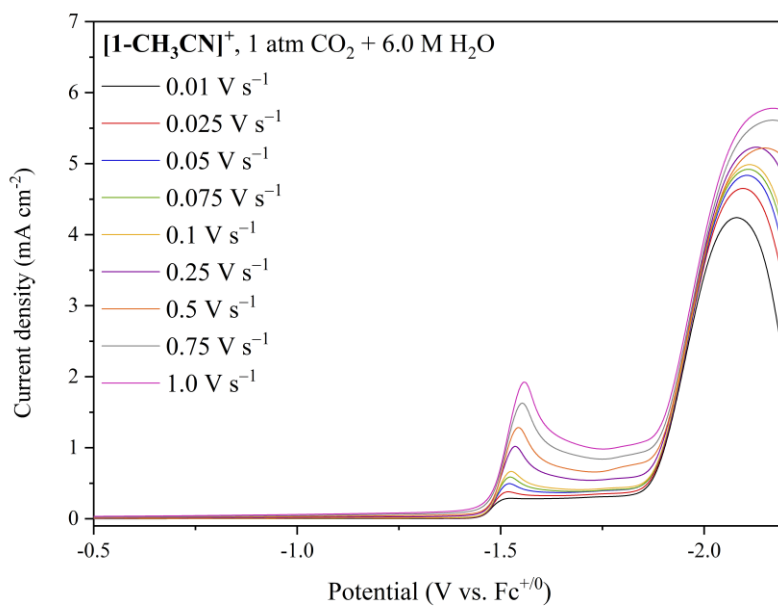


Figure ESI-29. (top) Overlay of scan rate dependent linear sweep voltammograms of $[1\text{-CH}_3\text{CN}]^+$ recorded at 1 mM catalyst concentration in 0.1 M $[\text{Bu}_4\text{N}][\text{PF}_6]$ acetonitrile supporting electrolyte at a glassy carbon disc electrode under 1 atm CO_2 with 6.4 M H_2O . (bottom) Scatter plot of TOF vs scan rate to estimate the TOF_{max} of $[1\text{-CH}_3\text{CN}]^+$ at high overpotential (-2.11 V).

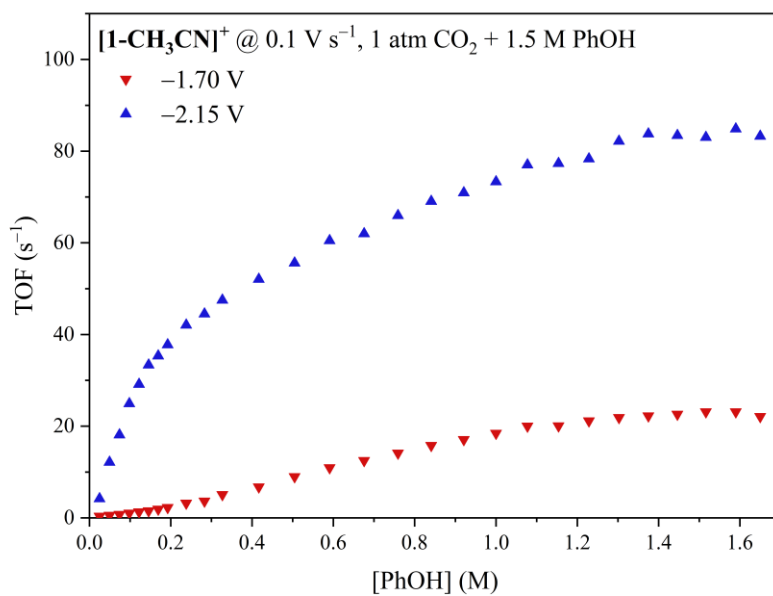
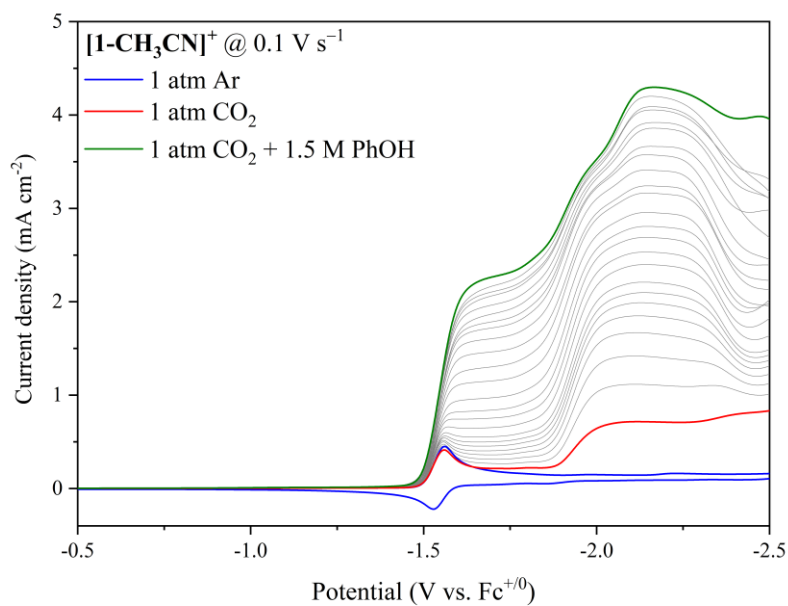


Figure ESI-30. (top) Linear sweep voltammetry of $[1\text{-CH}_3\text{CN}]^+$ recorded at 1 mM catalyst concentration in 0.1 M $[\text{Bu}_4\text{N}][\text{PF}_6]$ acetonitrile supporting electrolyte at a glassy carbon disc electrode with a scan rate (ν) of 0.1 V s^{-1} under 1 atm CO_2 with increasing PhOH concentration. (bottom) Scatter plot of TOF vs $[\text{PhOH}]$ determined at low (-1.70 V) and high (-2.15 V) overpotentials.

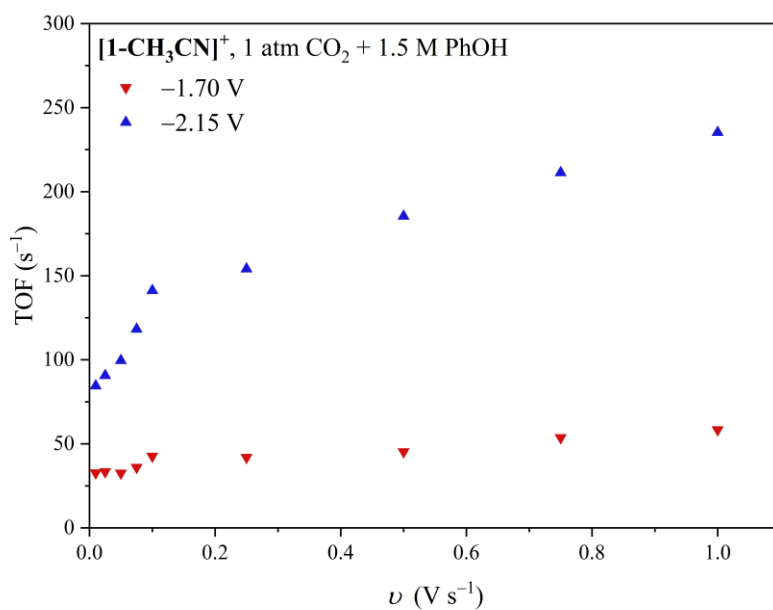
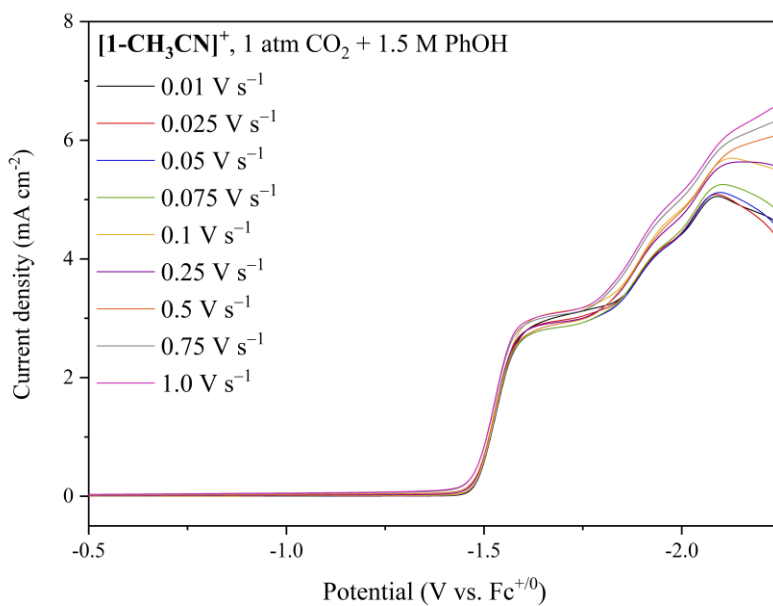


Figure ESI-31. (top) Overlay of scan rate dependent linear sweep voltammograms of [1-CH₃CN]⁺ recorded at 1 mM catalyst concentration in 0.1 M [Bu₄N][PF₆] acetonitrile supporting electrolyte at a glassy carbon disc electrode under 1 atm CO₂ with 1.5 M PhOH. (bottom) Scatter plot of TOF vs scan rate to estimate the TOF_{max} of [1-CH₃CN]⁺ at low (-1.70 V) and high (-2.15 V) overpotentials.

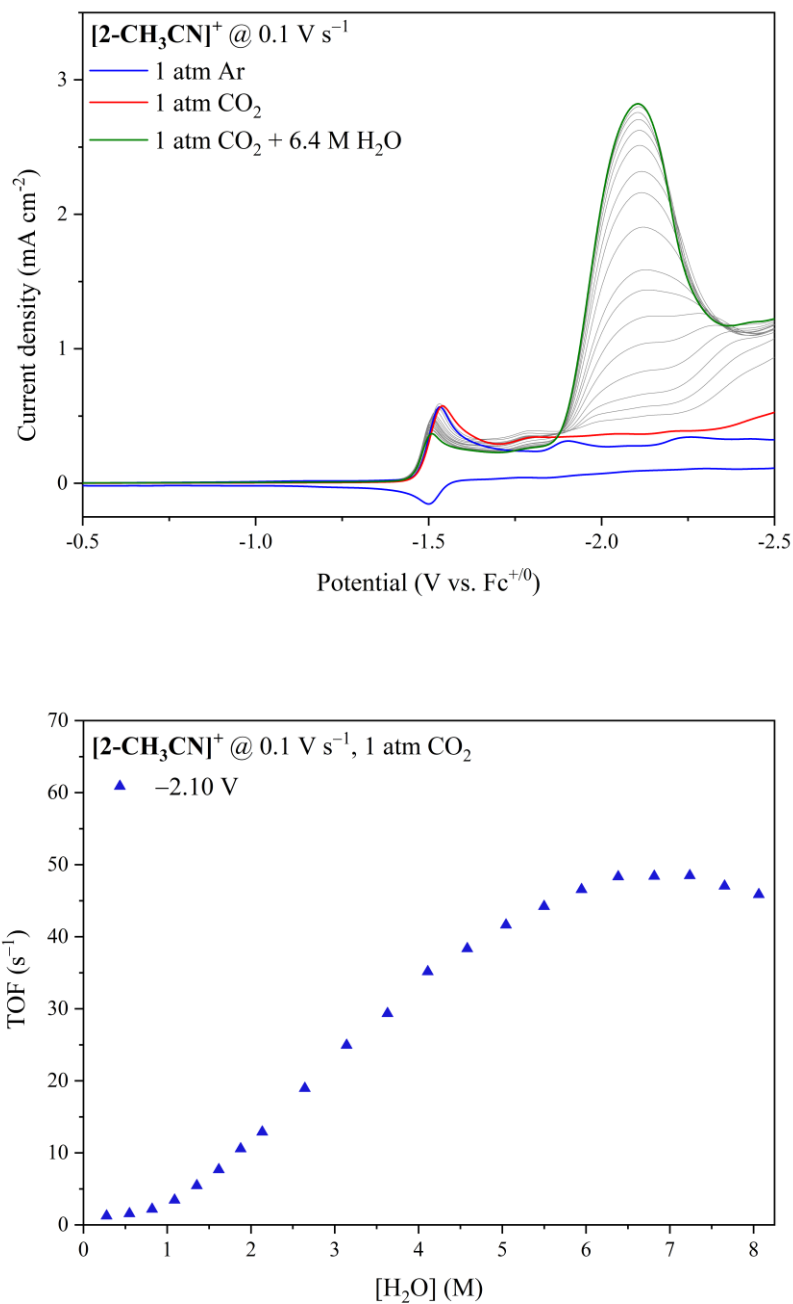


Figure ESI-32. (top) Linear sweep voltammetry of [2-CH₃CN]⁺ recorded at 1 mM catalyst concentration in 0.1 M [Bu₄N][PF₆] acetonitrile supporting electrolyte at a glassy carbon disc electrode with a scan rate (ν) of 0.1 V s⁻¹ under 1 atm CO₂ with increasing H₂O concentration. (bottom) Scatter plot of TOF vs [H₂O] determined at high overpotential (-2.10 V).

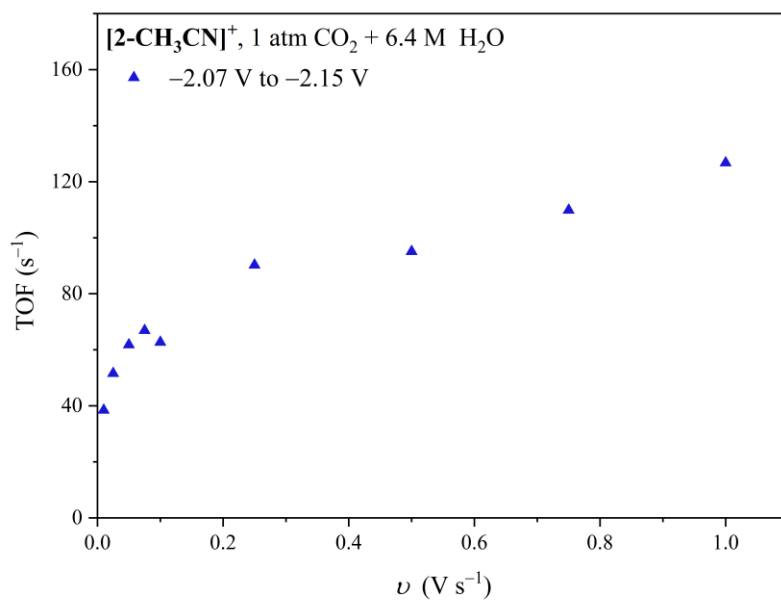
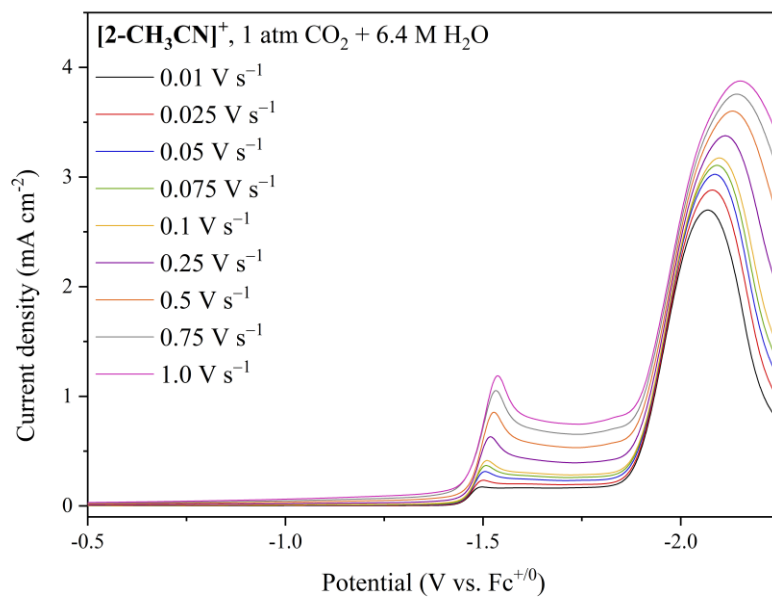


Figure ESI-33. (top) Overlay of scan rate dependent linear sweep voltammograms of $[2\text{-CH}_3\text{CN}]^+$ recorded at 1 mM catalyst concentration in 0.1 M $[\text{Bu}_4\text{N}][\text{PF}_6]$ acetonitrile supporting electrolyte at a glassy carbon disc electrode under 1 atm CO_2 with 6.4 M H_2O . (bottom) Scatter plot of TOF vs scan rate to estimate the TOF_{max} of $[2\text{-CH}_3\text{CN}]^+$ at high overpotential (-2.07 to -2.15 V).

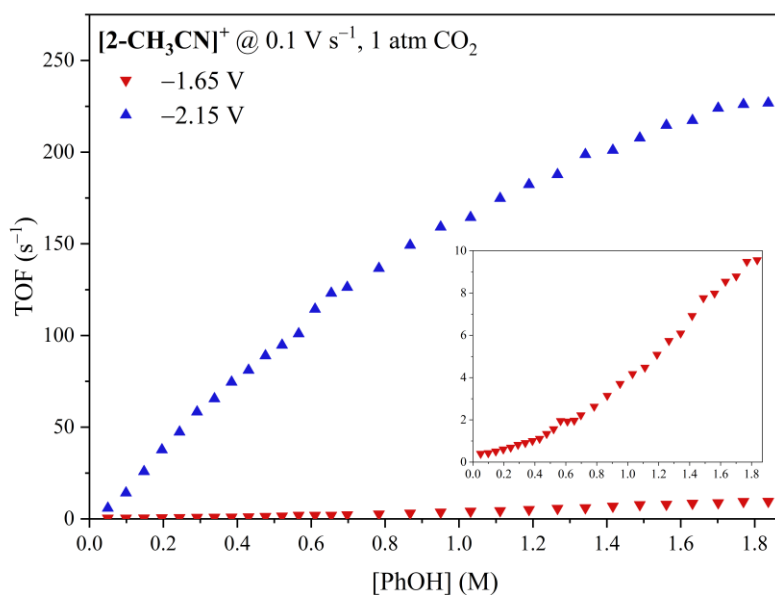
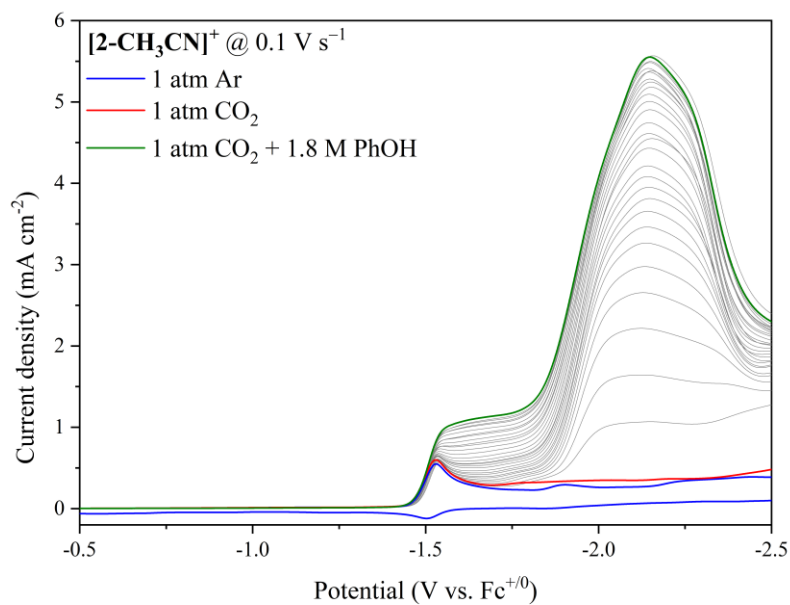


Figure ESI-34. (top) Linear sweep voltammetry of **[2-CH₃CN]⁺** recorded at 1 mM catalyst concentration in 0.1 M **[Bu₄N][PF₆]** acetonitrile supporting electrolyte at a glassy carbon disc electrode with a scan rate (ν) of 0.1 V s⁻¹ under 1 atm CO₂ with increasing PhOH concentration. (bottom) Scatter plot of TOF vs **[PhOH]** determined at low (-1.65 V) and high (-2.15 V) overpotentials.

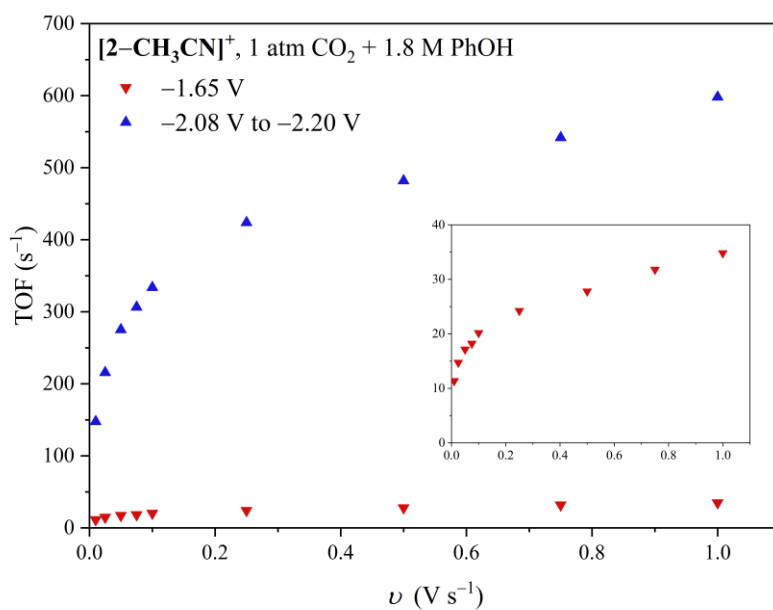
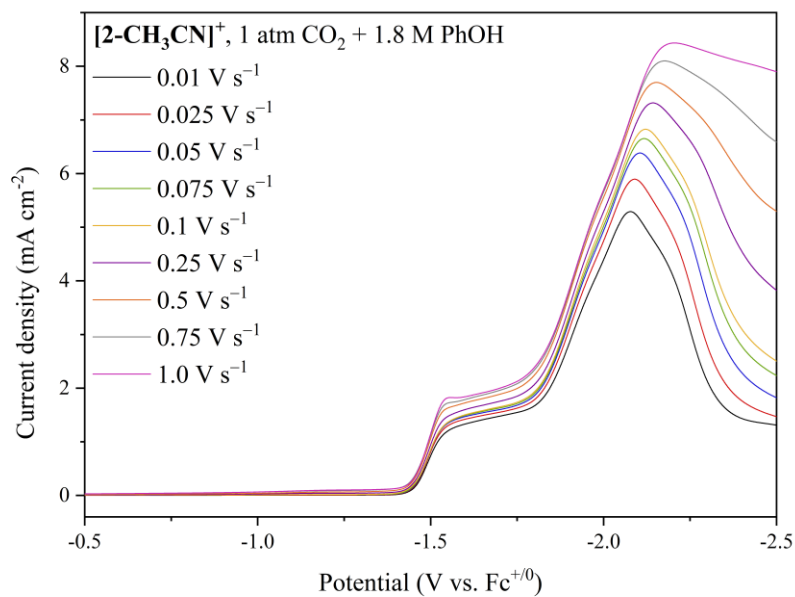


Figure ESI-35. (top) Overlay of scan rate dependent linear sweep voltammograms of $[2\text{-CH}_3\text{CN}]^+$ recorded at 1 mM catalyst concentration in 0.1 M $[\text{Bu}_4\text{N}][\text{PF}_6]$ acetonitrile supporting electrolyte at a glassy carbon disc electrode under 1 atm CO_2 with 1.5 M PhOH. (bottom) Scatter plot of TOF vs scan rate to estimate the TOF_{max} of $[2\text{-CH}_3\text{CN}]^+$ at low (-1.65 V) and high (-2.08 to -2.20 V) overpotentials.

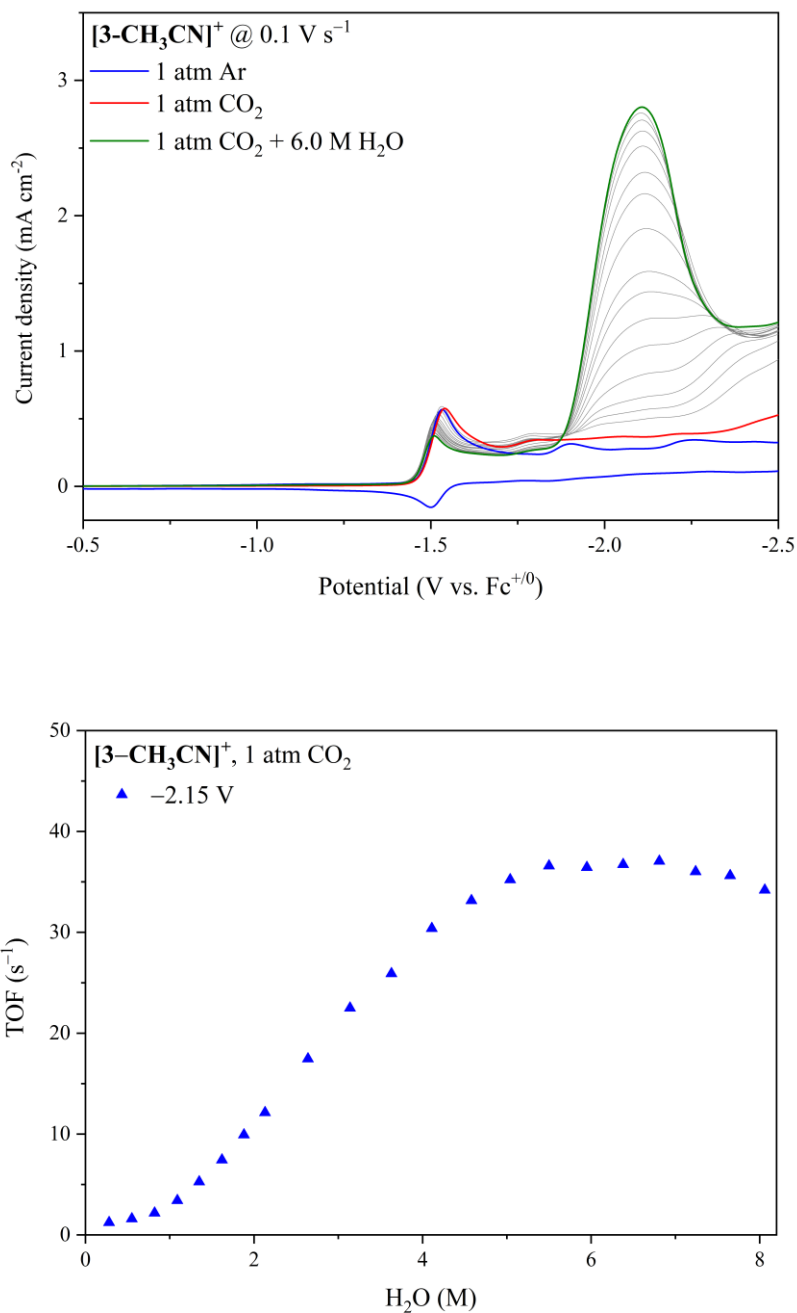


Figure ESI-36. (top) Linear sweep voltammetry of $[3\text{-CH}_3\text{CN}]^+$ recorded at 1 mM catalyst concentration in 0.1 M $[\text{Bu}_4\text{N}][\text{PF}_6]$ acetonitrile supporting electrolyte at a glassy carbon disc electrode with a scan rate (ν) of 0.1 V s^{-1} under 1 atm CO_2 with increasing H_2O concentration. (bottom) Scatter plot of TOF vs $[\text{H}_2\text{O}]$ determined at -2.15 V . Steady state conditions and hence TOF_{max} are confirmed below by scan-rate dependence with optimum H_2O concentration.

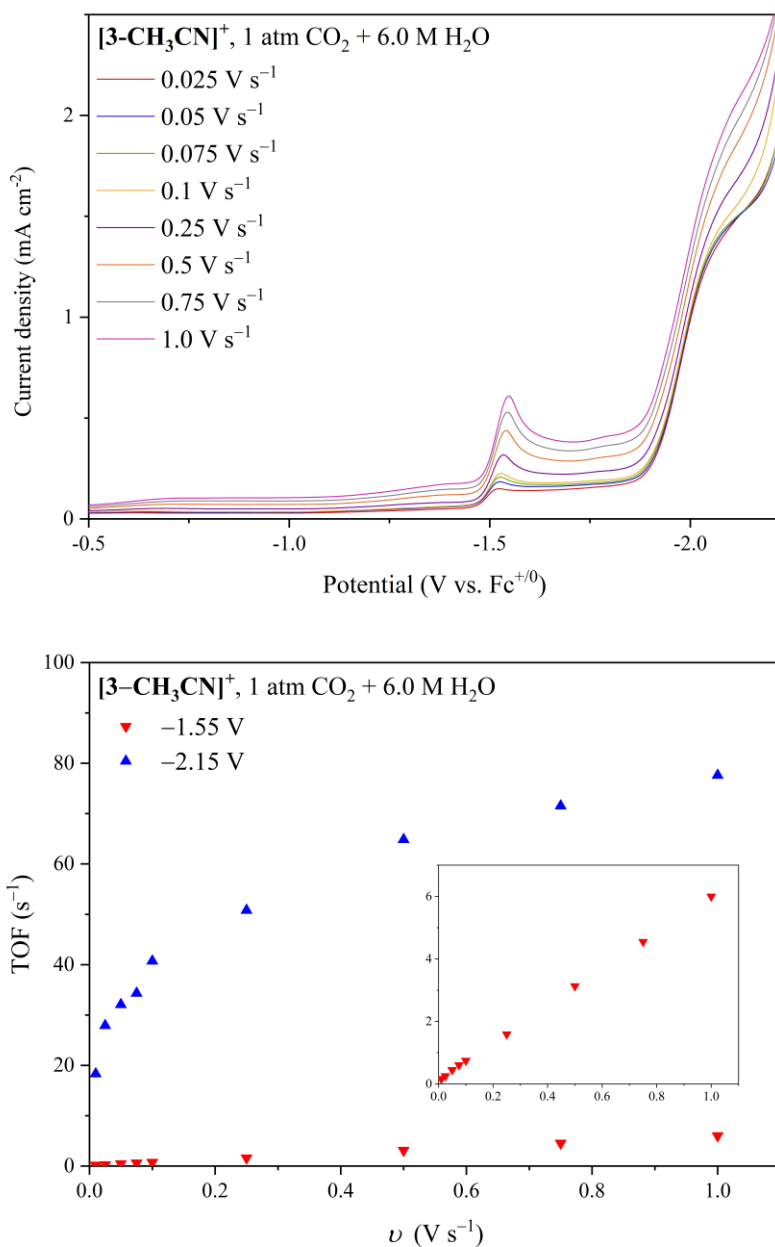


Figure ESI-37. (top) Overlay of scan rate dependent linear sweep voltammograms of [3-CH₃CN]⁺ recorded at 1 mM catalyst concentration in 0.1 M [Bu₄N][PF₆] acetonitrile supporting electrolyte at a glassy carbon disc electrode under 1 atm CO₂ with 6.4 M H₂O. (bottom) Scatter plot of TOF vs scan rate to estimate the TOF_{max} of [3-CH₃CN]⁺ at low (-1.55 V) and high (-2.15 V) overpotentials.

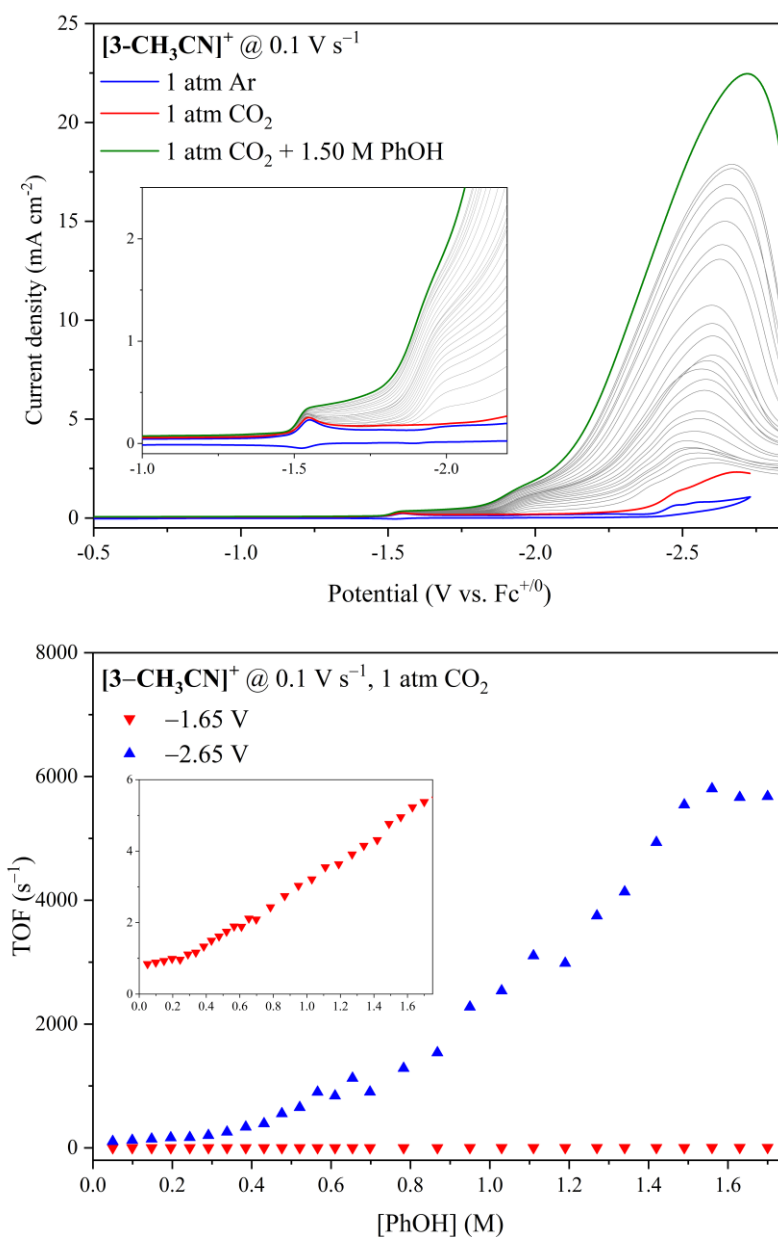


Figure ESI-38. (top) Linear sweep voltammetry of $[3\text{-CH}_3\text{CN}]^+$ recorded at 1 mM catalyst concentration in 0.1 M $[\text{Bu}_4\text{N}][\text{PF}_6]$ acetonitrile supporting electrolyte at a glassy carbon disc electrode with a scan rate (ν) of 0.1 V s^{-1} under 1 atm CO_2 with increasing PhOH concentration. (bottom) Scatter plot of TOF vs $[\text{PhOH}]$ determined at low (-1.65 V) and high (-2.65 V) overpotentials. Steady state conditions and hence TOF_{max} are confirmed below by scan-rate dependence with optimum PhOH concentration.

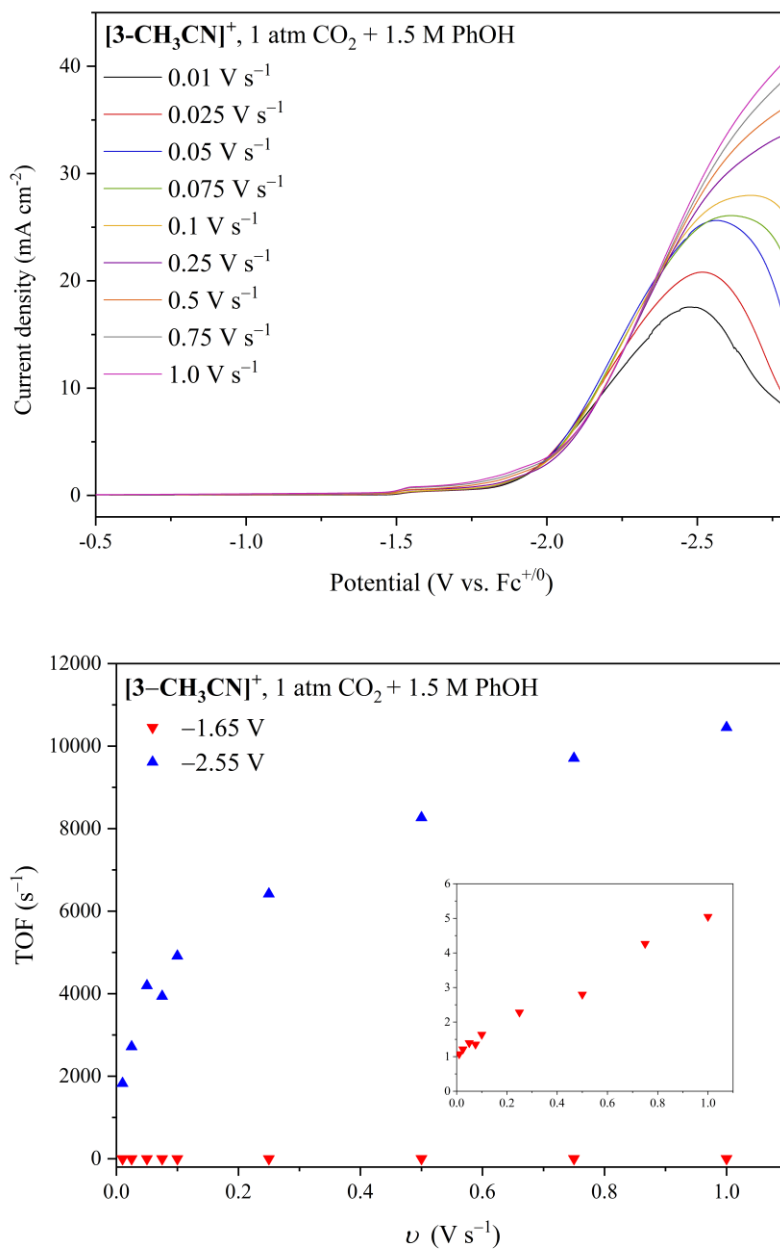


Figure ESI-39. (top) Overlay of scan rate dependent linear sweep voltammograms of [3-CH₃CN]⁺ recorded at 1 mM catalyst concentration in 0.1 M [Bu₄N][PF₆] acetonitrile supporting electrolyte at a glassy carbon disc electrode under 1 atm CO₂ with 1.5 M PhOH. (bottom) Scatter plot of TOF vs scan rate to estimate the TOF_{max} of [3-CH₃CN]⁺ at low (-1.65 V) and high (-2.55 V) overpotentials.

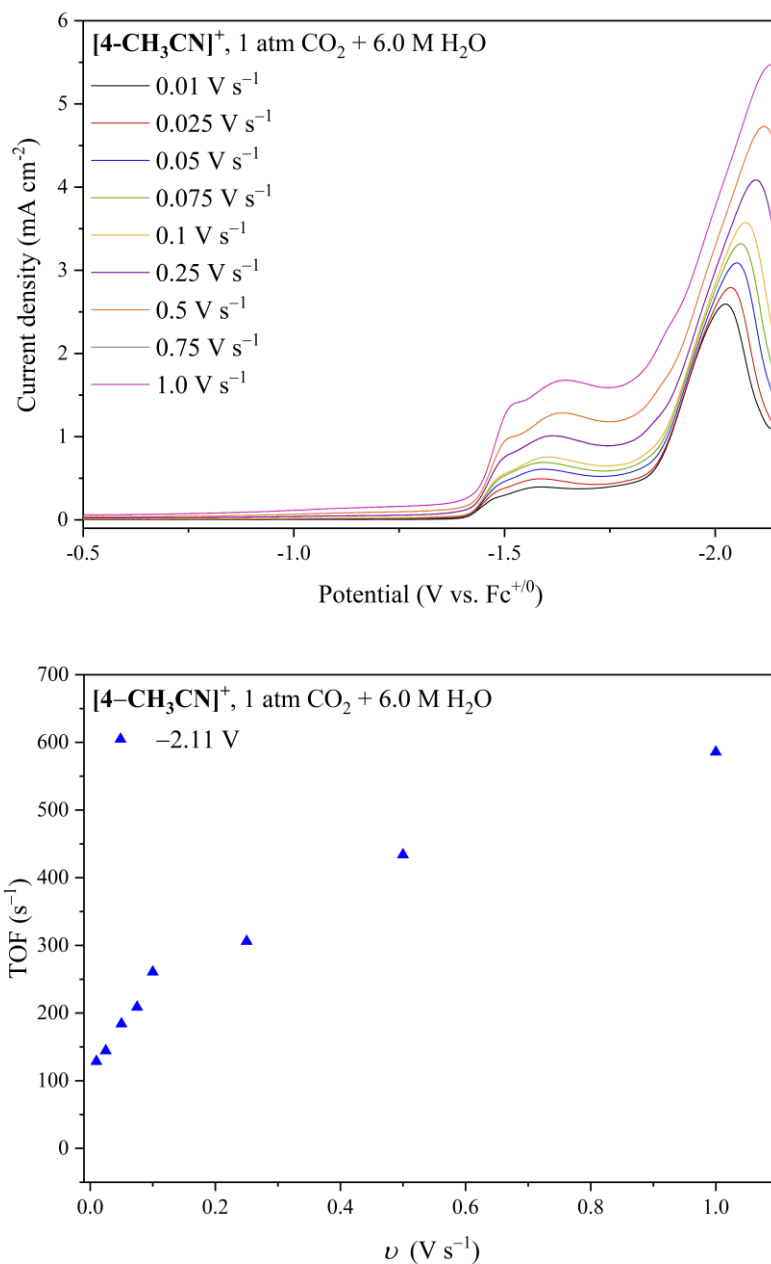


Figure ESI-40. (top) Overlay of scan rate dependent linear sweep voltammograms of [4-CH₃CN]⁺ recorded at 1 mM catalyst concentration in 0.1 M [Bu₄N][PF₆] acetonitrile supporting electrolyte at a glassy carbon disc electrode under 1 atm CO₂ with 6.0 M H₂O. (bottom) Scatter plot of TOF vs scan rate to estimate the TOF_{max} of [4-CH₃CN]⁺ at high overpotential (-2.11 V).

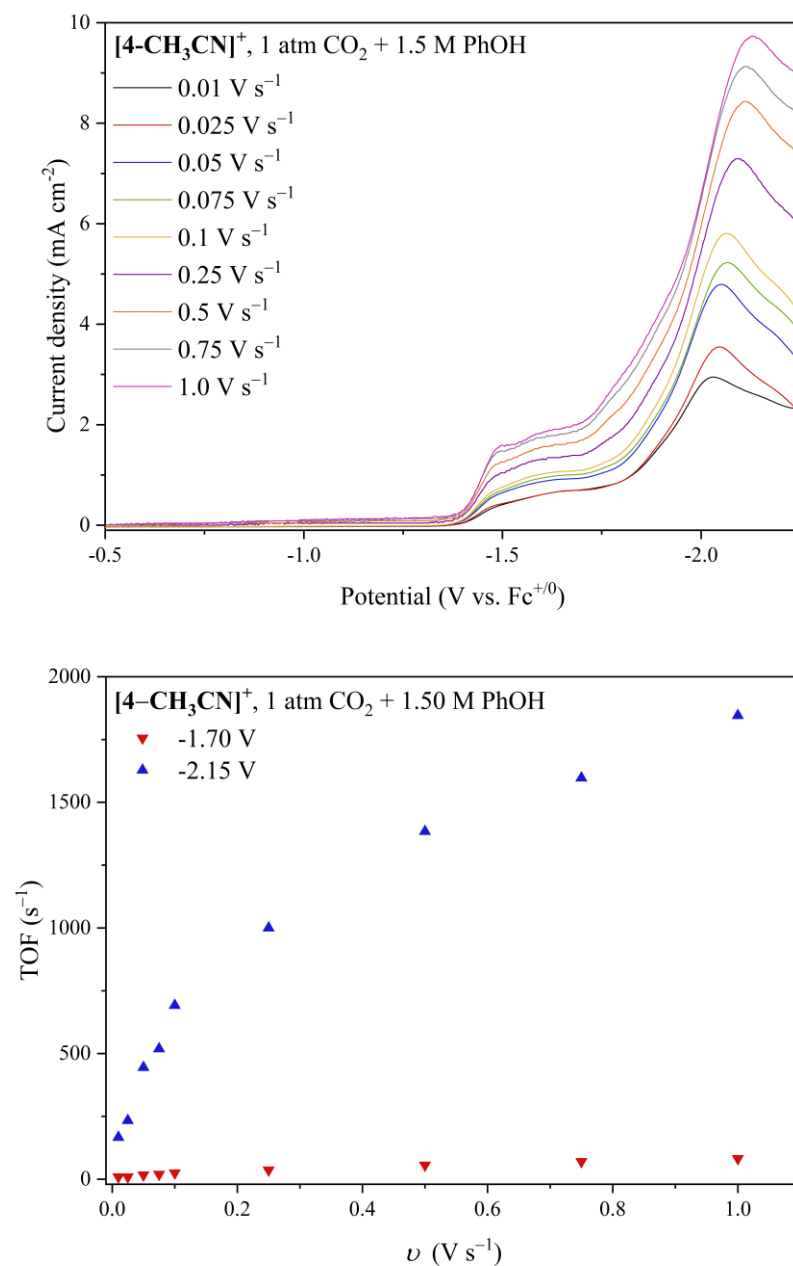


Figure ESI-41. (top) Overlay of scan rate dependent linear sweep voltammograms of [1-CH₃CN]⁺ recorded at 1 mM catalyst concentration in 0.1 M [Bu₄N][PF₆] acetonitrile supporting electrolyte at a glassy carbon disc electrode under 1 atm CO₂ with 1.5 M PhOH. (bottom) Scatter plot of TOF vs scan rate to estimate the TOF_{max} of [1-CH₃CN]⁺ at low (-1.70 V) and high (-2.15 V) overpotentials.

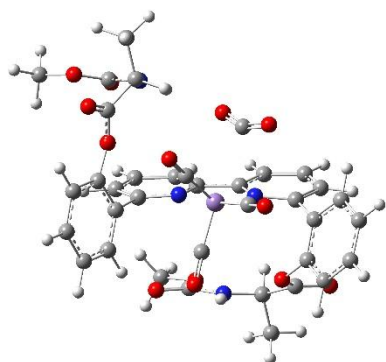
8. Computational data and transition state structures.

Table ESI-1. Summary of computed activation enthalpy (ΔH^\ddagger) and free energy of activation (ΔG^\ddagger) values in kcal/mol for selected kinetic steps in Scheme 2 for PhOH as the Brønsted acid source. The ΔH^\ddagger values are presented in parentheses.

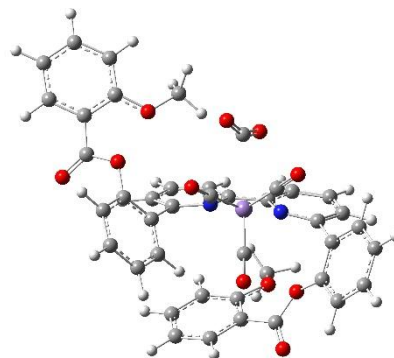
	Separated Reactants ^a		Reactant Complex ^a	
	[2-CH ₃ CN] ⁺	[3-CH ₃ CN] ⁺	[2-CH ₃ CN] ⁺	[3-CH ₃ CN] ⁺
[Mn-CO₂]⁻ Formation	9.3 (1.2)	7.4 (1.3)	7.2 (9.3)	4.0 (5.4)
[Mn-H] Formation	15.4 (1.7)	19.6 (7.3)	11.7 (9.6)	11.9 (10.4)
HCO₂⁻ Formation (Insert – ET)	12.9 (5.4)	11.6 (4.3)	9.3 (6.1)	13.5 (9.9)
HCO₂⁻ Formation (ET– Insert)	11.8 (4.2)	11.1 (4.0)	6.9 (4.7)	9.8 (7.7)
H₂ Formation (Insert – ET)	19.8 (8.2)	<i>b</i>	12.6 (10.9)	<i>b</i>
H₂ Formation (ET– Insert)	17.4 (4.7)	17.0 (6.3)	13.8 (11.3)	15.8 (14.6)

^a We employed two approaches in the prediction of activation enthalpy (ΔH^\ddagger) and free energy of activation (ΔG^\ddagger) values; one assuming fully separated reactants in solution (labelled as Separated Reactants; TS structures shown below) and the other in reference to a reactant complex (labelled as Reactant Complex).

^b A transition state structure could not be optimized for this pathway.

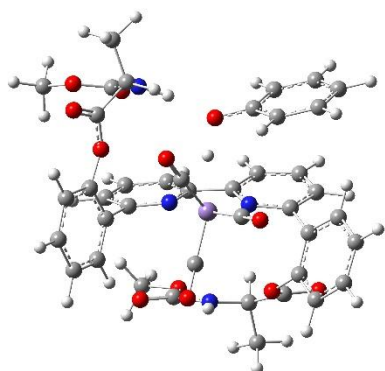


[2]⁻ + CO₂

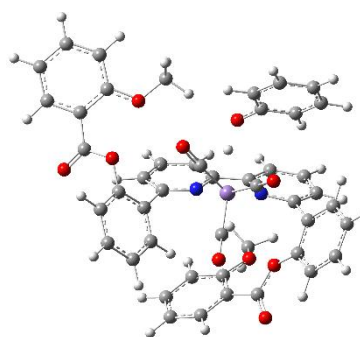


[3]⁻ + CO₂

Figure ESI-42. Optimized transition state structures for CO₂ binding at [2]⁻ and [3]⁻.

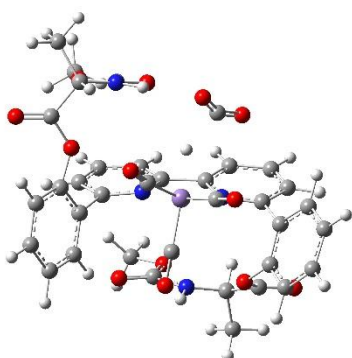


[2]⁻ + PhOH

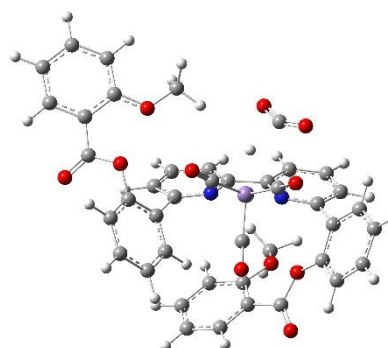


[3]⁻ + PhOH

Figure ESI-43. Optimized transition state structures for protonation of [2]⁻ and [3]⁻ by PhOH.

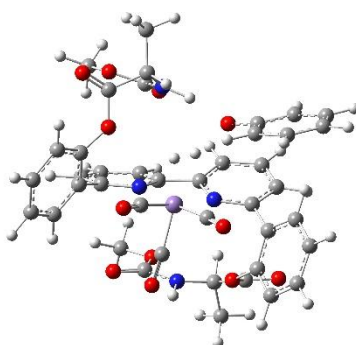


[2-H] + CO₂



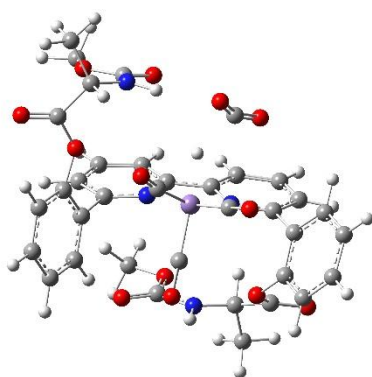
[3-H] + CO₂

Figure ESI-44. Optimized transition state structures for CO₂ insertion at [2-H] and [3-H].

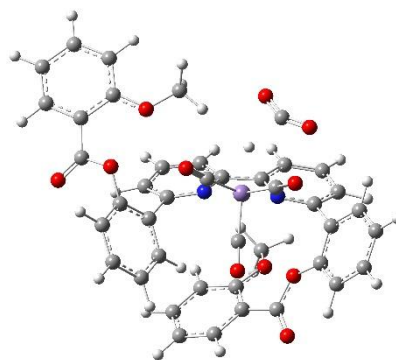


[2-H] + PhOH

Figure ESI-45. Optimized transition state structure for protonation of [2-H] by PhOH.

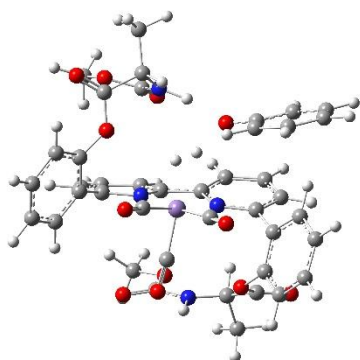


[2-H]⁻ + CO₂

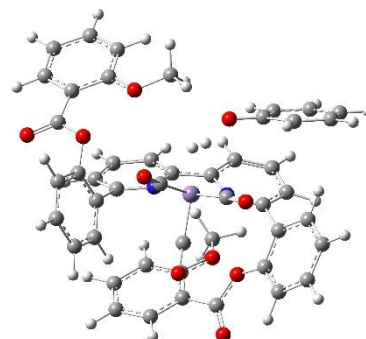


[3-H]⁻ + CO₂

Figure ESI-46. Optimized transition state structures for CO₂ insertion at [2-H]⁻ and [3-H]⁻.



[2-H]⁻ + PhOH



[3-H]⁻ + PhOH

Figure ESI-47. Optimized transition state structures for protonation of [2-H]⁻ and [3-H]⁻ by PhOH.

9. References

1. M. Bourrez, F. Molton, S. Chardon-Noblat and A. Deronzier, *Angew. Chem. Int. Ed.*, 2011, **50**, 9903-9906.
2. G. R. Fulmer, A. J. M. Miller, N. H. Sherden, H. E. Gottlieb, A. Nudelman, B. M. Stoltz, J. E. Bercaw and K. I. Goldberg, *Organometallics*, 2010, **29**, 2176-2179.
3. V. Blaszczak, A. Murphy, L. Suntrup, K. T. Ngo, B. Reed, S. Groysman, D. C. Grills and J. Rochford, *ChemCatChem*, 2024, **16**.
4. T. Scheiring, W. Kaim and J. Fiedler, *J. Organomet. Chem.*, 2000, **598**, 136-141.
5. H. S. Yu, X. He, S. L. Li and D. G. Truhlar, *Chem. Sci.*, 2016, **7**, 5032-5051.
6. A. V. Marenich, C. J. Cramer and D. G. Truhlar, *J. Phys. Chem. B*, 2009, **113**, 6378-6396.
7. F. Weigend and R. Ahlrichs, *Phys. Chem. Chem. Phys.*, 2005, **7**, 3297-3305.
8. Frisch M. J. et al., Gaussian Inc., Wallingford, CT., Revision A.1 edn., 2009.
9. C. J. Cramer, *Essentials of Computational Chemistry: Theories and Models*, John Wiley & Sons, Chichester, 2004.
10. D. C. Grills, M. Z. Ertem, M. McKinnon, K. T. Ngo and J. Rochford, *Coord. Chem. Rev.*, 2018, **374**, 173-217.